

IMPERIAL

EMBEDDED SYSTEM FOR NEAR FIELD COMMUNICATION

Author

B.E. TOWNLEY

CID: 02457041

Supervised by

DR O. SYDORUK

A Thesis submitted in fulfillment of requirements for the degree of
Master of Science in Communications and Signal Processing

Department of Electrical and Electronic Engineering
Imperial College London
2024

Abstract

Near Field Communication (NFC) is a widely used technology, known for its short-range capabilities and common applications such as contactless payment cards. However, NFC's potential extends beyond these traditional short range uses, and recent research has begun to explore its capabilities in a broader range of scenarios, such as weather stations [1] and wireless charging [2]. The commercial NFC systems currently available are not able to meet the demands for many of the emerging applications. Therefore, this thesis presents the design of a bespoke and highly adaptable NFC system that follows the ISO 15693 standard. The bespoke system designed in this report can aid in the development of new applications, as it can be easily adapted for optimal performance in a wide variety of NFC systems.

This thesis explores various receiver architectures designed to exploit the extended read range of the ISO 15693 standard. Specifically, it explains the development and implementation of a Vicinity Coupling Device (VCD) that is controlled by a low cost microcontroller. The versatility of this VCD was demonstrated by adapting it to estimate the location of the Vicinity Integrated Circuit Card (VICC) along a travelling wave antenna. This is possible as after the VICC performs load modulation, the reflected and transmitted signals must travel different distances within the antenna before being extracted from their respective outputs. This causes a delay between the two signals that can be exploited to form a classification system which assigns delay values to particular loops of the antenna.

The results demonstrate that with 0.09 W of power supplied to an inductive loop, and an undersampling factor of 13, a read range of up to 11 cm is achievable. However, when the entire detection system was conducted digitally, the maximum read range decreased to 8 cm. Additionally, with loops spaced 20 cm apart within a travelling wave antenna consisting of nine loops, a sampling rate of 10 MHz was found to result in a classification error rate of 3.06% when localising a VICC to the nearest loop. When a low cost microcontroller was used to implement the localisation system, using the data from every other loop to form a classification system led to an error rate of 15%. This error rate reduced to 0.28% if the data from only every fourth loop was used to form a classification system.

Declaration of Originality

I hereby declare that the work presented in this thesis is my own unless otherwise stated. To the best of my knowledge the work is original and ideas developed in collaboration with others have been appropriately referenced.

Copyright Declaration

The copyright of this thesis rests with the author and is made available under a Creative Commons Attribution Non-Commercial No Derivatives licence. Researchers are free to copy, distribute or transmit the thesis on the condition that they attribute it, that they do not use it for commercial purposes and that they do not alter, transform or build upon it. For any reuse or redistribution, researchers must make clear to others the licence terms of this work.

Acknowledgments

I would like to thank Dr Oleksiy Sydoruk, for agreeing to take me as his student and providing unmatched mentorship throughout the duration of this dissertation. I would not have been able to achieve the standard of results without his guidance.

I thank my partner Amy, whose support and reassurance encouraged me to achieve standards to the best of my ability, never settling for anything less than I knew I could accomplish.

And finally, I would like to thank my parents for both their constant support, and financial sacrifices that have enabled me to be here and achieve my goals.

Contents

Abstract	i
Declaration of Originality	iii
Copyright Declaration	v
Acknowledgments	vii
List of Acronyms	xi
List of Figures	xiii
1 Introduction	1
1.1 Introduction	1
1.2 Aims and Objectives	3
2 Literature Review	5
2.1 Background	5
2.2 Localisation	9
2.3 Overview of The ISO 15693 Protocol	10
3 Implementation of Receiving Architectures	13
3.1 Hardware	13
3.2 Signal Received From Vicinity Integrated Circuit Card (VICC)	15
3.3 Undersampling and Digital Filtering	19
3.4 Working Principles of The Designed Receivers	21
3.5 Results and Analysis	29
4 Localisation	33
4.1 Hardware and Received Signals	33
4.2 Localisation Techniques	36
4.3 Results and Analysis	38
Conclusions	47

A Scattering Parameters of Hardware	49
-------------------------------------	----

Bibliography	53
--------------	----

List of Acronyms

AM Amplitude Modulation

SOF Start Of Frame

EOF End Of Frame

UID Unique Identifier

ADC Analogue to Digital Converter

SNR Signal to Noise Ratio

RFID Radio Frequency Identification

BER Bit Error Rate

VICC Vicinity Integrated Circuit Card

VCD Vicinity Coupling Device

BPF Band-Pass Filter

NFC Near Field Communication

FFC Far Field Communication

TDOA Time Difference of Arrival

MI Magneto Inductive

ASK Amplitude Shift Keying

NRZ Non Return to Zero

HF High Frequency

FDR Fisher's Discriminant Ratio

List of Figures

1.1 NFC system block diagram	2
2.1 diagram showing reactive near field, radiative near field, and far field	6
2.2 inductive coupling between VCD and VICC	8
2.3 Diagram showing how analogue frequencies get mapped to digital frequencies after sampling	8
2.4 unmodulated signal for transmission of 1 and 0 from VICC to VCD	11
3.1 Block diagram of RFID system	14
3.2 Photograph of RFID system in laboratory	14
3.3 Signal output from coupler and it's frequency spectrum	16
3.4 Signal read by oscilloscope both before and after digital filtering	17
3.5 Signal read from the analogue notch filter both before and after digital filtering . .	18
3.6 Signal output by detector and sampled by the oscilloscope	18
3.7 Example of different methods to filter the signal read from the	19
3.8 frequency spectrum of signal sampled using the STM32 board	20
3.9 Undersampled signal after digital filtering	21
3.10 Undersampled signal received from detector	22
3.11 Flowchart which shows general behaviour of all implemented receivers	23
3.12 EOF transmitted by the VICC	24
3.13 Flow chart for threshold receiver	25
3.14 Subcarrier load modulation sequence performed by the VICC when transmitting a logic 1	26
3.15 Flow chart for correlation receiver which works alongside an AM detector.	26
3.16 Flow chart for the second method of amplitude detection	27
3.17 Flow chart for the first method of amplitude detection	28
3.18 Flow chart for the correlation receiver without an AM detector	29
3.19 BER vs distance when no detector is used	30
3.20 BER vs distance when an AM detector is used	31
3.21 BER vs distance, when detector is used and carrier wave has 5V amplitude . . .	32

3.22 BER vs distance for the '1 out of 4' and '1 out of 256' coding modes	32
4.1 Picture of the travelling wave antenna	34
4.2 Block diagram of localisation system	34
4.3 Signal read by oscilloscope when localising VICC	35
4.4 First state transition of the signal read by the oscilloscope when localising the VICC	36
4.5 TDOA measured at each loop plotted against the loop number it was measured at	39
4.6 Confusion matrices for cross-correlation and thresholding when performing localisation on data sampled at 10 MHz	40
4.7 Error rate against sampling frequency when all nine loops of the travelling wave antenna were used	41
4.8 Error rate against sampling frequency when only 3 and 5 of the travelling wave antennas loops were used	41
4.9 Fishers discriminant ratio against sampling rate when all 9 loops of the antenna are used	42
4.10 Fishers discriminant ratio against sampling rate when only 3 and 5 loops of the antenna are used	43
4.11 Frequency polygons for the TDOA measurements at each loop when measured using thresholding	44
4.12 Confusion matrices for localisation using thresholding on STM32 board	44
4.13 Frequency polygon for the TDOA measurements at each loop made using cross-correlation	45
4.14 Confusion matrices for localisation using cross-correlation on the STM32 board . .	46
A.1	50
A.2	50
A.3	51

1

Introduction

Contents

1.1 Introduction	1
1.2 Aims and Objectives	3

1.1 Introduction

Near Field Communication (NFC) has become integral in day-to-day life for people in the UK, in applications ranging from contactless payment cards to production lines in major factories. NFC is a type of High Frequency (HF) Radio Frequency Identification (RFID) system operating at 13.56 MHz, which enables data transfer between devices over small distances. The block diagram in Figure 1.1 shows an NFC system. It is a form of bidirectional half-duplex communication between a master device and a slave. In this report, the master is referred to as the VCD, while the slave is referred to as the VICC. These devices are more commonly known as a reader and tag/transponder, however, the notation used in the ISO 15693 standard is followed here. An important aspect of NFC systems is that energy is transmitted from the VCD to the VICC. This occurs due to inductive coupling between the coils of each device, allowing both passive and active VICCs to be used. Passive VICCs do not have a battery and draw power from the magnetic field created by the VCD, while active VICCs have their own power source. Passive VICCs provide a plethora of advantages and are one of the main reasons NFC has become so popular. Batteries are expensive to produce, environmentally unfriendly once discarded [3], and after time must be replaced or

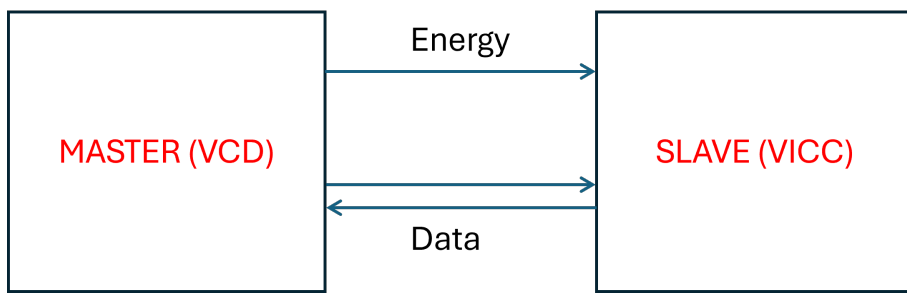


Figure 1.1: Block diagram of an NFC system with master transmitting energy and data to the slave

recharged. Therefore, creating a portable electronic device which does not require a battery is appealing to manufacturers. The energy harvesting capabilities of NFC can be implemented in smart ways to reduce the overall energy usage in an electronic device [1], [4], another important benefit in the energy driven world of today.

Due to this wide array of benefits, new applications for NFC are constantly being devised, such as weather stations [1], navigation [5], and wireless charging [2]. While there is a large selection of standard solutions available to purchase, none provide the flexibility required for many of these emerging applications. As such, systems must be designed that allow for bespoke control of transmission and reception. This project aimed to design and implement such a system, and then analyse different methods, both hardware and software, of demodulating the received signal into a series of bits. A travelling wave antenna was then employed to allow both message demodulation and VICC localisation to be conducted.

Testing was conducted using a digital oscilloscope to capture the data, and MATLAB to process it. The STM32 NUCLEO-F446RE development board was then implemented to create an embedded RFID system. This low-cost microcontroller was programmed using the C language to implement a practical receiving/transmitting system, compliant with the ISO 15693 standard.

Different types of VCD were implemented, with each offering distinct advantages. All designs remained highly adaptable, allowing new applications to easily modify the VCD to optimise its performance. On the software side, threshold, correlation, and amplitude receivers were implemented alongside digital filtering. In hardware, an Amplitude Modulation (AM) detector and a notch filter were implemented to provide a wide variety of potential solutions.

To conclude the project, an application of NFC was tested, in which the VCD was used to determine the location of the VICC. A travelling wave antenna which consisted of nine loops was used to provide two outputs. A Time Difference of Arrival (TDOA) occurred between the outputs

due to the waves travelling different distances after modulation by the VICC, and before being read by the VCD. A classification system was developed using a decision tree, allowing the position of a VICC to be estimated to the nearest loop based on the delay measured.

1.2 Aims and Objectives

This project aims to implement and test a bespoke NFC system that can be easily adapted for different applications. The value of a custom NFC system is then highlighted by using it to estimate the location of a VICC. Initially, a VCD was designed that followed the ISO 15693 standard and could elicit a response from a VICC. Once a response was received, it was analysed using a digital oscilloscope and MATLAB. This analysis allowed different types of receiver to be designed and implemented in C. These C programs were loaded onto a microcontroller and used to decode the VICC's response into a Unique Identifier (UID). The different receivers were then tested to evaluate the strengths and weaknesses of each. The single inductive loop was then replaced with a travelling wave antenna consisting of nine inductive loops. This antenna was used to estimate the position of a VICC using both thresholding and cross-correlation. Finally, a classification system was formed to assign each TDOA measurement to the nearest loop.

In order for these aims to be achieved, the project's objectives are as follows:

- Create a transmitter that can operate according to the ISO 15693 standard.
- Implement different types of receiver ensuring all can resolve the VICC's UID.
- For all receiver designs, measure the Bit Error Rate (BER) for different distances between the VCD and the VICC.
- Use an oscilloscope to capture TDOA data that allows all 9 loops to be classified.
- Test the accuracy of localisation for different sampling rates and different numbers of classes.
- Implement the localisation system on a low cost microcontroller.

2

Literature Review

Contents

2.1 Background	5
2.2 Localisation	9
2.3 Overview of The ISO 15693 Protocol	10

2.1 Background

Commercial wireless communication systems are dominated by Far Field Communication (FFC). However, with the advent of new technologies and the ever-increasing read ranges, NFC has become a more powerful technology. This has led to its wide adoption in mobile phones and contactless payment systems, along with many new applications [5]–[7], including ticketing systems [8] and weather stations [1].

The near field region can be divided into two sections: the reactive near field and the radiating near field. Figure 2.1 shows the three main regions of an EM wave. The reactive near field is the area immediately surrounding the antenna, where the EM fields store and release energy rather than propagating away as EM waves [9], [10]. The radiating near field is where the EM waves are propagating away from the antenna but have not yet formed into planar waves and must still be modelled as spherical. The far field is where the EM waves can be characterised as planar. The type of NFC implemented in this project is solely based on the magnetic component of the reactive near field.

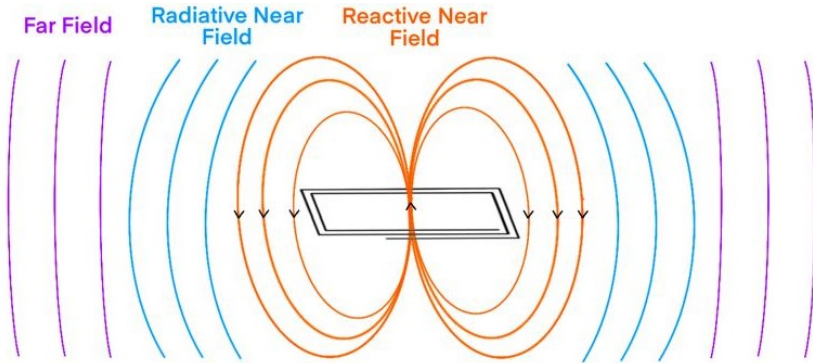


Figure 2.1: The structure of the EM wave/field in the reactive near field, radiative near field, and far field

The size of the reactive near field is determined by the Fresnel distance, which is calculated using equation 2.1, where D refers to the maximum aperture dimension of the antenna, and λ represents the wavelength [11]. This formula provides an absolute limit on the distance achievable with an NFC system and indicates the two possible ways to increase the near field distance: raising the frequency, or increasing the antenna aperture. In the next generation of mobile communications, a frequency of 6 GHz will be used alongside Extremely Large Antenna Arrays (ELAA), resulting in a large near field region [12]. At lower frequencies such as 13.56 MHz, Magneto Inductive (MI) waves have been used to increase the antenna size [13], allowing a travelling wave MI antenna to achieve a read range greater than 0.5 metres.

$$\frac{D}{2} \left(\frac{D}{\lambda} \right)^{1/3} \quad (2.1)$$

While the distance of the near field may increase, the field strength in this region decays at a rate of $1/d^3$ [14]. Therefore, the VCD requires a high power to obtain a large read range, making energy efficiency crucial. Beamforming is a technique used in multiple-input and multiple-output (MIMO) systems to direct energy flow in a specific direction. Beamforming has been used in FFC communication for over 25 years [15], and more recently, researchers have been implementing it into NFC systems, allowing increased data rates [16], and improving the energy efficiency of the system [17].

Despite the wide range of benefits that accompany NFC systems, there are still significant challenges that need to be overcome. Currently, the primary use of NFC is in contactless payment cards, meaning significant security measures must be put in place [18]. With ever-increasing methods being developed to extend the read range [13], [19], the risk of relay attacks is growing.

A relay attack occurs when an eavesdropper uses a device to bridge the gap between a VICC and VCD, allowing them to complete some action without the owner's knowledge [20].

Another drawback of NFC is that the current possible data rates are lower than those used in competing technologies. The two main standards used in NFC are ISO 14443 and ISO 15693, which define standard data rates of 106 kbytes/s and 26.48 kbytes/s respectively. In comparison, Bluetooth offers data rates of 1 or 3 Mbytes/s, and home Wi-Fi can reach 2.5 Gbytes/s, making these technologies more practical than NFC for transmitting large amounts of data. Encryption usually increases the size of the data, therefore, the amount of encryption that can be performed in NFC systems may be limited by the data rate. While research has been conducted with the aim of increasing the transmission rate [21], [22], this often results in a decrease in the read range.

One of the most important parameters of the antenna used in an NFC system is the Quality (Q) factor. This can be calculated using the formula $Q = f/B$, where B is the bandwidth of the resonant circuit, and f is the resonant frequency of the antenna [14]. For the VICC, a high Q factor is desirable, as this ensures a large energy transfer range between the VCD and the VICC. For the VCD however, the small bandwidth associated with a large Q factor has detrimental effects on signal reception. When subcarrier load modulation is used, sidelobes are created around the carrier frequency that contain the information for demodulation. These sidelobes should not be attenuated by the antenna, therefore, a minimum bandwidth around the resonant frequency must be maintained to ensure the subcarrier-induced sidelobes are not affected. A decrease in bandwidth also results in a reduction of the channel capacity, and thus limits the data rate possible [22]. Therefore, when designing an NFC system, the increase in power provided by a large Q factor must be balanced against the possible attenuation of the sidebands and lower channel capacity that occur due to the resulting smaller bandwidth. Consequently, the optimal Q factor is dependent on the subcarrier frequency, the required data rate, and the expected read range in a given application.

When in the near field, inductive coupling occurs between the primary coil in the VCD and the secondary coil in the VICC, as shown in Figure 2.2. This allows the VICC to affect the magnetic field generated by the VCD through load modulation [23]. By switching a load on and off, the VICC controls how much energy it draws from the magnetic field, causing a change in the voltage at the VCD's antenna. By carefully controlling the switching, a message is transmitted via Amplitude Shift Keying (ASK) without the VICC transmitting any signal itself.

To reduce the errors in signal demodulation, many NFC systems implement load modulation with a subcarrier [24]. The amplitude changes caused by the load modulation generate sidebands

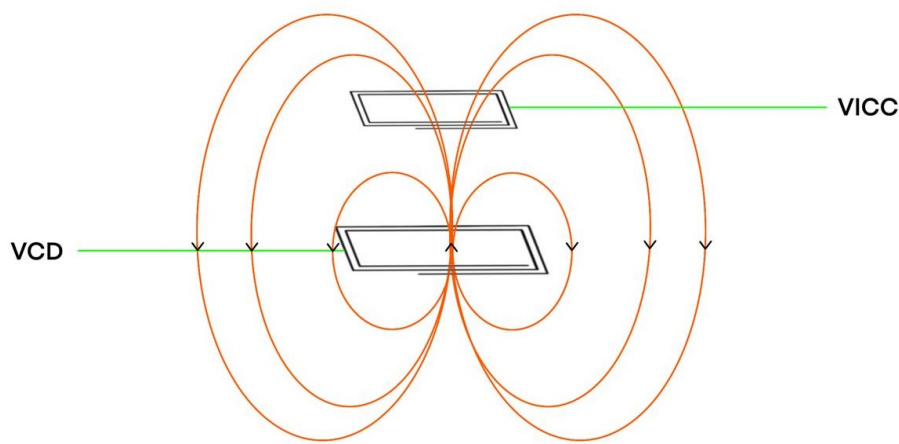


Figure 2.2: Inductive coupling between the VCD and VICC with magnetic lines shown

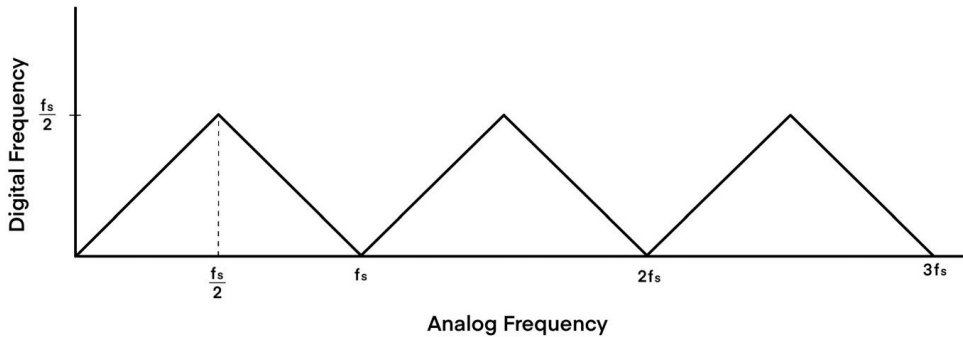


Figure 2.3: Diagram showing how analogue frequencies get mapped to digital frequencies after sampling. Nyquist's sampling rate is depicted as $f_s/2$

around the carrier frequency of the VCD's signal. If the load is also switched on and off at a higher frequency, f_s , then spectral lines are created in the sidebands of the carrier frequency, f_c , at frequencies of $f_c - f_s$ and $f_c + f_s$. These two spectral lines carry identical information, which allows the signal to be demodulated into the transmitted message.

According to Nyquist's sampling theorem, a signal must be sampled at a frequency at least twice its own to avoid aliasing [25]. When aliasing occurs, frequencies over Nyquist's rate are mapped to a frequency under it, as shown in Figure 2.3, where Nyquist's rate is depicted as $f_s/2$. This means that while an Analogue to Digital Converter (ADC) is unable to measure frequencies over half its sampling rate, the information contained within these frequencies is not lost, instead, it is mapped to a new frequency. Aliasing can cause significant interference if two peaks in the analogue spectrum are mapped to similar frequencies. For this reason, an anti-aliasing filter can be implemented before sampling to remove unwanted high frequencies. In this project, sampling was conducted both above and below Nyquist's rate.

2.2 Localisation

In 1999 the US government mandated that all emergency service callers should have their precise location automatically determined [26]. This mandate sparked a plethora of UHF long distance localisation techniques to be designed [27]. Developments in UHF RFID based localisation quickly followed, these predominantly use the received signal strength to estimate a devices location [28]. There has been no such catalyst for the development of localisation systems working in the HF range, thus in comparison HF RFID based localisation is still in its infancy.

HF RFID based localisation has been heavily used in robotics. A robot can self-localise by connecting with one of multiple VICCs that have been placed around a room [29], [30]. A similar technology has been implemented in libraries to help find books. Xu *et al.* [31] created a robot capable of traversing bookshelves while scanning each shelf to locate a desired book. There has also been work on fabricating antenna arrays that can be used to localise a VICC. Mehlman *et al.* [32] designed an antenna array that could be printed into everyday appliances such as a table, allowing objects placed on top to be tracked.

Travelling wave antennas are designed to prevent the formation of standing waves. After travelling through the antenna, the signal is terminated through an impedance matched load. This stops a wave reflecting off the boundary and interfering with the forward wave to create a standing wave [33]. This project used a travelling wave antenna consisting of nine conductive loops. When the VICC modulates the carrier wave at a loop, sidebands are created, which are added to both the signal transmitted by the loop and the signal reflected back from it [13]. As such, a different version of the modulated signal can be read at either end of the antenna. Depending on the location of the VICC along the antenna, the reflected and transmitted MI waves need to travel different distances before being output from the antenna. This results in a TDOA between the two signals which can be converted into a distance if the signals group velocity is known. This method of localisation was first proposed by Syms *et al.* [34] using a MI wave antenna, and later expanded upon by Voronov *et al.* [35] to include a variety of waveguide antenna topologies. This section of the report is closely related to the work conducted by Syms *et al.*, but has some key differences. Here, the ISO 15693 standard will be used, while ISO 14443 was previously implemented. A key element of this work is implementing a VCD onto a readily available microcontroller, therefore, a low complexity threshold system was implemented and compared with a cross-correlator.

2.3 Overview of The ISO 15693 Protocol

The ISO 15693 standard operates on a request and response basis, the VICC only transmits a response after it has received a request from the VCD [36]. Transmission errors are detected using a two byte cyclic redundancy check. Each message begins with a Start Of Frame (SOF) and finishes with an End Of Frame (EOF). These delimiters consist of code sequences that were previously considered invalid.

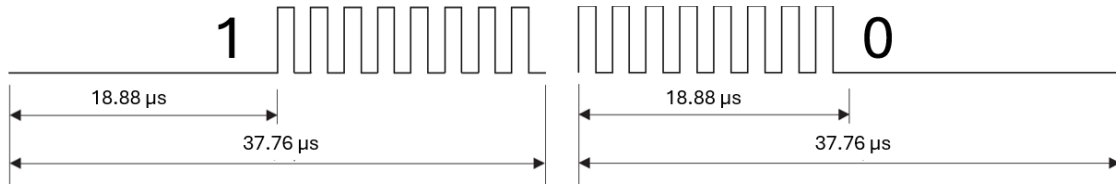
In the ISO 15693 standard, the VICC requires a magnetic field in the range of 0.15-5 A/m rms [37]. This results in an increased read range when compared to ISO 14443, where the tag requires a minimum of 1.5 A/m rms to power up [38].

To maximise the power supplied to the VICC, the message transmitted by the VCD should be in the high state for as long as possible, and minimise the amplitude change when going from the high state to the low state. Therefore, the bit coding method and the modulation rate will affect the amount of power transmitted. The maximum power is achieved in ISO 15693 by combining pulse position modulation with 10% ASK. While 10% ASK can be implemented in ISO 14443, it is only possible in combination with Non Return to Zero (NRZ) coding [38], requiring the signal to be in the low state for longer than if pulse position modulation was used. This further demonstrates the additional read range capabilities of ISO 15693.

For communication from the VCD to the VICC, ASK is used with a modulation index of either 100% or 10%. Pulse position modulation is used to transmit the bits of the message [37]. A pause, defined as a period of time during which the carrier amplitude is at the low level, is placed at a specific point in a time frame, informing the VICC of the transmitted bit sequence.

The VCD chooses between '1 out of 256' and '1 out of 4' coding modes [37]. '1 out of 256' coding works by having a single pause in one of 256 possible positions in a frame, the location where the pause occurs gives the value of the transmitted byte. Here, the data rate is 1.66 kbits/s, with the important property of maximising the time the ASK signal is in the high state. '1 out of 4' coding works by having the pause at one of four possible positions in a frame, with each frame transmitting two bits of information. This mode has a data rate of 26.48 kbits/s , which is fifteen times higher than that of the '1 out of 256' mode.

The combination of coding type and modulation index must be selected depending on the application of the NFC system. Pairing '1 out of 256' coding with 10% modulation is considered



2

Figure 2.4: Manchester coded signal for transmission of a logic 0 and a logic 1 from VICC to VCD. The timings shown are for the fast data rate

the long distance mode, as this maximises the power transmitted to the VICC. Pairing '1 out of 4' coding with 100% ASK is considered the fast data mode. 100% ASK is easier for the VICC to demodulate, making it preferable for short distances where the energy supplied is still sufficient.

The VICC transmits information to the VCD via subcarrier load modulation combined with Manchester coding [37]. There is a choice between low and high data rates, with all time periods divided by four for the high data rate. Figure 2.4 shows the unmodulated signal transmitted by the VICC for logic 0 and logic 1. One of the main aims of this project was to find different ways to accurately demodulate the received signal into bit periods that consist of one of the two signals shown in Figure 2.4.

The high data rate is 26.48 kbit/s, and the low data rate is 6.62 kbit/s [37]. For long read range applications the low data rate should be used, as this will result in stronger subcarrier frequencies and allow the receiver to collect more samples for demodulation. ISO 14443 has higher data rates available, the nominal rate is 106 kbit/s, and after initialisation and anti-collision this rate can be further multiplied by 2, 4, 8, 16, 32 or 64 [38].

Both standards use subcarrier load modulation for communication from the VICC to the VCD. However, they use different subcarrier frequencies, ISO 14443 uses a frequency of 847 kHz [38], which is higher than the 423.75 kHz subcarrier used in ISO 15693 [37]. Consequently, the sidebands created by the subcarrier are two times further from the strong carrier frequency when using ISO 14443. This makes the information carrying frequencies easier to isolate, as there are less strict requirements on the Band-Pass Filter (BPF) implemented to remove the unwanted frequencies. The advantage of a smaller subcarrier frequency is that the antenna used requires a smaller bandwidth, allowing a larger Q factor. This results in more power being transmitted to the VICC, and thus an increased read range for ISO 15693 systems when compared to ISO 14443.

Table 2.1 gives an overview of the two different standards.

	ISO 14443		ISO 15693
	Part A	Part B	
VCD -> VICC			
Bit coding	Modified Miller	NRZ	Pulse Position Modulation
Modulation	ASK 100%	ASK 10%	ASK 10 or 100 %
Baud rate	106 kbits/s	106 kbits/s	26.48 or 1.65 kbits/s
VICC -> VCD			
Bit coding	Manchester	NRZ	Manchester
Subcarrier modulation	ASK	BPSK	ASK or FSK
Subcarrier frequency	847 kHz	847 kHz	423 kHz
Baud rate	106 kbits/s	106 kbits/s	26.48 or 6.62 kbits/s

Table 2.1: An overview of the main elements of the ISO 14443 [38] and ISO 15693 standards [37][36]

3

Implementation of Receiving Architectures

Contents

3.1 Hardware	13
3.2 Signal Received From Vicinity Integrated Circuit Card (VICC)	15
3.3 Undersampling and Digital Filtering	19
3.4 Working Principles of The Designed Receivers	21
3.5 Results and Analysis	29

3.1 Hardware

The block diagram in Figure 3.1 illustrates the RFID system developed for this project. Figure 3.2 is a photograph showing the same RFID system once fully implemented in the laboratory. Some of the designed receivers conducted the detection entirely digitally, and so the analogue detector in Figure 3.1 was replaced with a notch filter. The oscilloscope was initially used for testing and analysis, but once this was completed, the ADC input pins of the STM32 board were used to collect the data.

A coupler was required to allow part of the signal at the antenna to be read by an ADC. The STM32 board generated a keyed signal that needed to be modulated with a 13.56 MHz carrier wave before transmission. To achieve this, a Mini-Circuits ZASWA-2-50DR+ high isolation switch

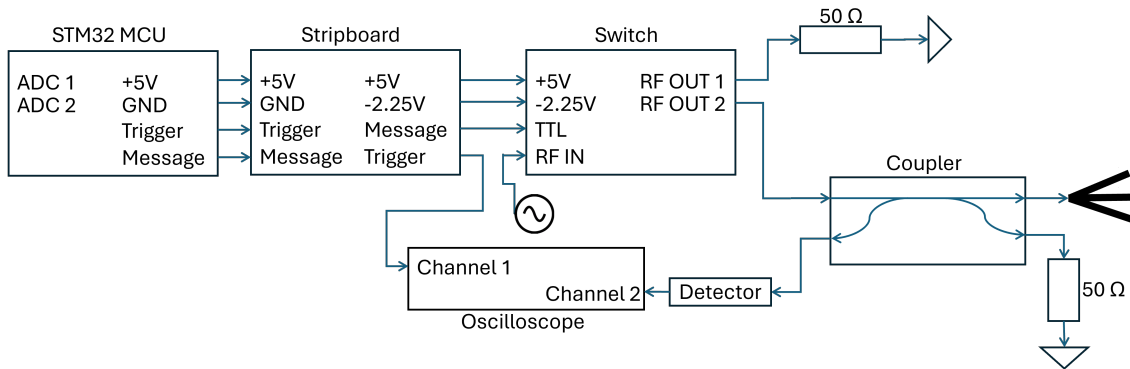


Figure 3.1: Block diagram of the RFID system used in this project

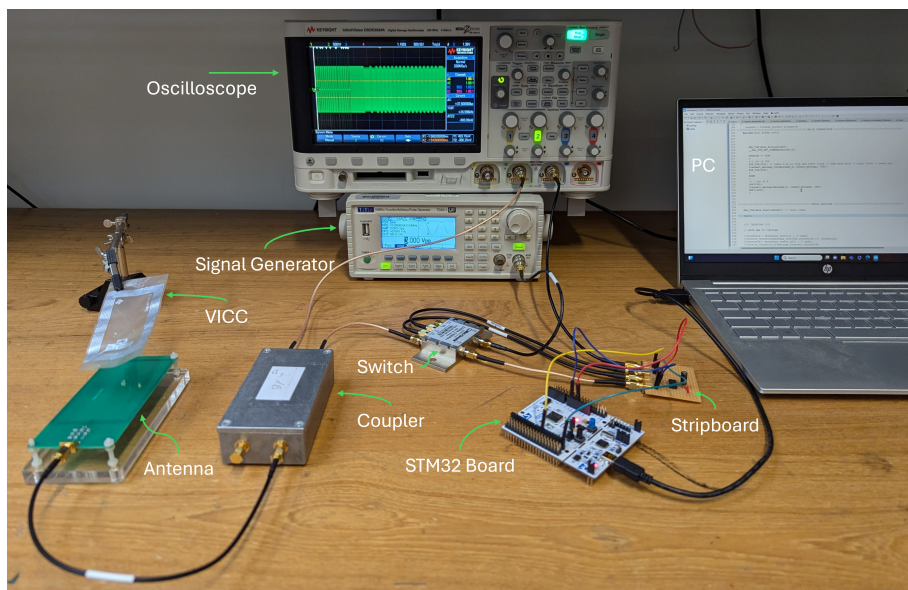


Figure 3.2: Labelled photograph of the laboratory configuration used for this project

was employed to create the modulated signal. The carrier wave was supplied by a TTi 50 MHz function generator, while DC power was provided by the STM32 board. A stripboard converted the signals generated by the STM32 board from jumper wires to SMA cables.

The STM32 NUCLEO-F446RE development board was used to control both the transmission and reception of the RFID system. The onboard ADC has a $50\text{ k}\Omega$ input impedance, and when a resolution of 12 bits was selected, the sampling rate was 1.64 MHz. The resolution could be increased to 15 bits, however, this results in a decrease in the sampling rate, which was found to negate any performance gains. The board has 14 independent timers, 5 of which were used in this project to ensure correct timings and test the efficiency of all code segments. Direct memory access (DMA) was implemented to transfer data directly from the ADC into memory, enabling all samples to be processed sequentially, regardless of the required processing time. The STM32 board was connected to a PC using the USB ports of each device. This connection allowed power to be supplied to the STM32 board and enabled data transfer between the two devices. C programs were sent from the PC to the STM32 board, and the VICC's UID was transmitted in the opposite direction.

3.2 Signal Received From Vicinity Integrated Circuit Card (VICC)

The STM32 board was programmed to transmit the inventory command to the VICC, which responds with its UID. This message consists of a SOF, followed by 96 bits of data, and concludes with an EOF. In this section, the signal received from the NFC system is sampled at a rate of 100 MHz using a digital oscilloscope. This signal is analysed to provide an overview of the signal output from the NFC system.

The VICC transmits information through subcarrier load modulation, with the subcarrier operating at 423.75 kHz. A sample of the signal output from the coupler is shown in Figure 3.3. Only a 2.5 ms section of the signal is displayed to highlight the modulated and unmodulated sections. The bottom plot of Figure 3.3 shows the frequency spectrum of the signal output from the coupler. The carrier signal is at 13.56 MHz, and there are two sidebands at 13.14 MHz and 13.99 MHz, that carry the necessary information for demodulation. The first two harmonics of the carrier signal have a magnitude within 5 dB of the information carrying sidebands. This could cause significant interference at the sideband frequencies if the signal is sampled at a rate below 41 MHz.

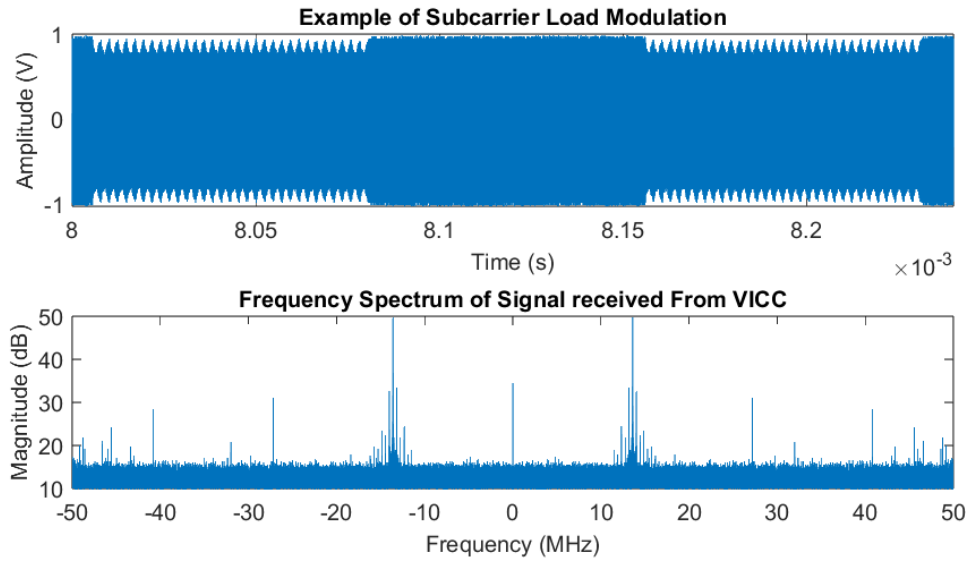


Figure 3.3: Top: 0.25ms of the signal output from the coupler. Bottom: The frequency spectrum of the signal output from the coupler. The signal was sampled at a rate of 100 MHz

Digital filtering was applied with the aim of removing all frequency components except those at 13.14 and 13.99 MHz, as they carry the information transmitted by the VICC. For the spectrum depicted in Figure 3.3, a digital BPF can isolate each of the sidebands. The top plot in Figure 3.4 presents a section of the signal output by the coupler, while the bottom plot displays the same signal post digital filtering. The 13.14 MHz and 13.99 MHz components were isolated using a 6th order BPF with a 400 kHz passband. The cyan plot represents the summation of these two filtered signals, whereas the orange plot represents only the 13.99 MHz component. Although in both cases the digital filtering has made the signal easier to demodulate, a significant component of the 13.56 MHz carrier wave remains after filtering.

A higher order BPF with a sharper transition bandwidth could enhance the attenuation of the carrier wave, however, this would increase the computational complexity. A more efficient method of removing the carrier wave is to implement an analogue notch filter. The top plot in Figure 3.5 shows the signal output from the notch filter, while the bottom plot displays the same signal after digital filtering. The load modulation has less effect in the top plot of Figure 3.5 when compared to the top plot of Figure 3.4. However, comparing the bottom plots of Figures 3.5 and 3.4 shows that the sideband frequencies are more effectively isolated by the digital filters when an analogue notch filter was employed. As a result, an amplitude demodulator would have fewer errors when processing this signal. It is important to note that when using the notch filter, the 13.99 MHz component is significantly stronger than the 13.14 MHz component. This occurs due to the non-

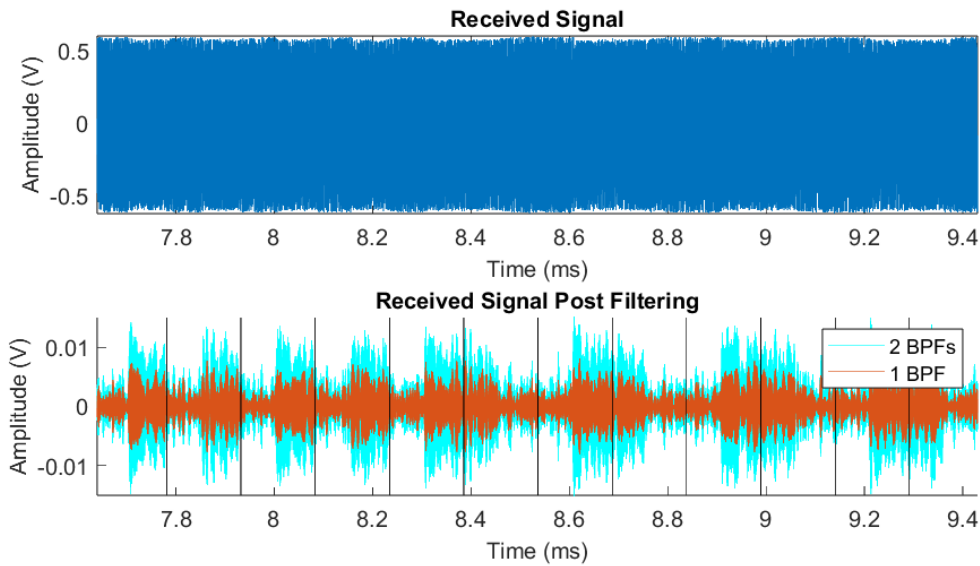


Figure 3.4: Top: Signal read by the oscilloscope directly from the coupler. Bottom: Signal output from the coupler after BPFs have been applied around the desired frequencies. The sampling rate was 100 MHz.

ideal performance of the notch filter, which attenuates the 13.14 MHz component. Therefore, in practical applications, if the upper sideband can be isolated without a high level of interference, then the 13.14 MHz component can be ignored, reducing the computational complexity, with minimal impact on the accuracy.

In order to reduce the demodulation error, an analogue AM detector was implemented to provide the envelope of the received signal. Figure 3.6 shows the output of the AM detector when the VICC is positioned 10 cm from the antenna. The detector raises the DC offset of the square wave during transmission, this can lead to issues with a threshold receiver if it is not properly adjusted. As the distance between the VCD and the VICC increases, the difference in amplitude between the high and low levels of the square wave decreases, until the AM detector can no longer identify the load modulation, and begins to output pure noise.

The AM detector demodulates the sideband frequencies. To reduce the number of errors that occur during demodulation, two methods of digital filtering were tested. The first method used a BPF to isolate the 423.75 kHz subcarrier, leaving the demodulator to distinguish between a 423.75 kHz sine wave and noise. The top plot in Figure 3.7 shows the signal output by the detector after applying the BPF. The second method focused on smoothing the signal received from the detector to create a more ideal square wave. The bottom plot in Figure 3.7 shows the signal output by the detector after applying a 6th order moving average filter. The second method of filtering is less

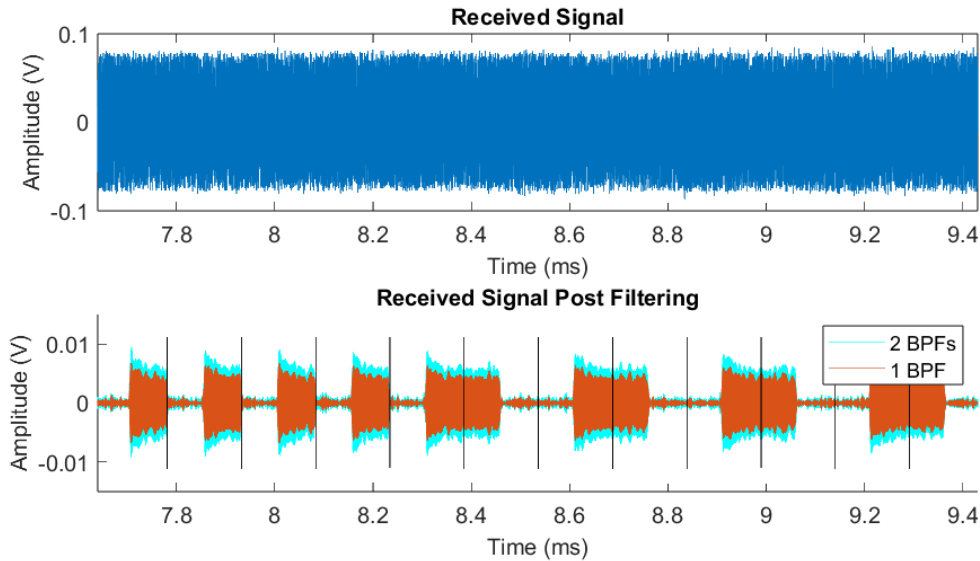


Figure 3.5: Top: Signal output from the notch filter. Bottom: Signal output from the notch filter after BPFs have been applied around the desired frequencies. The sampling rate was 100 MHz.

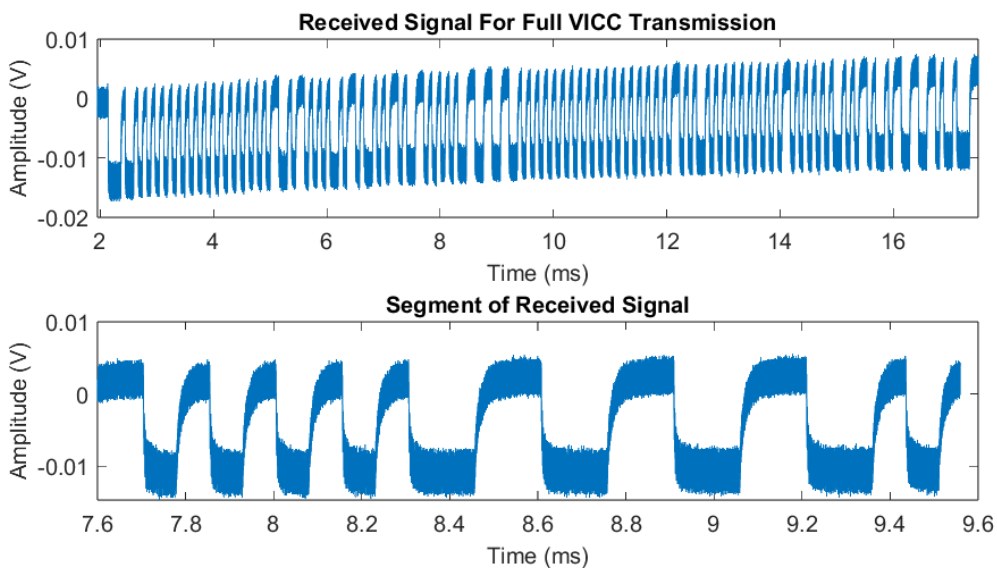


Figure 3.6: Top: The full signal output from the detector during VICC transmission. Bottom: 2ms of the signal output from the detector during VICC transmission. The sampling rate was 100 MHz.

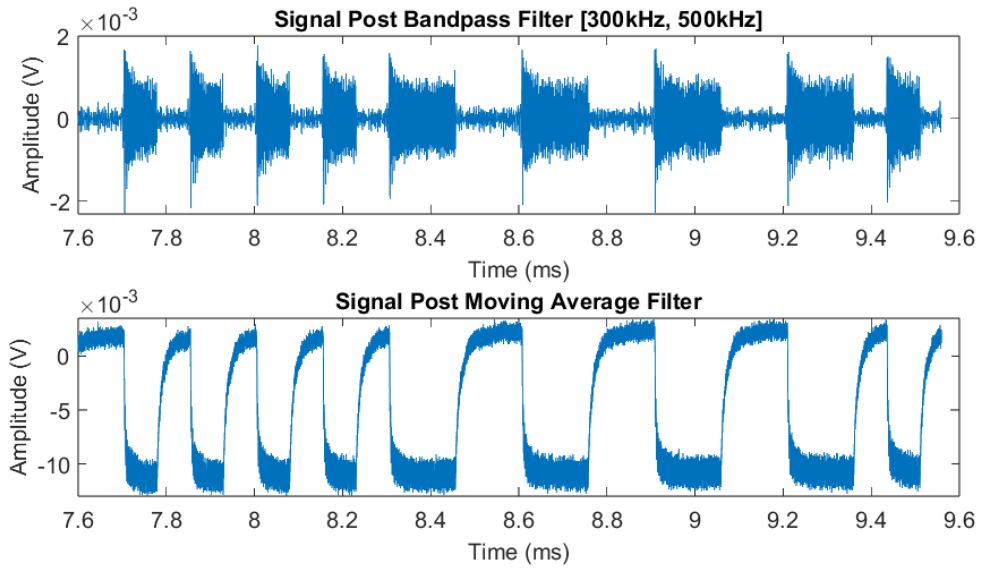


Figure 3.7: Top: Signal output by the detector after being filtered with a 6th order BPF with a center frequency of 423 kHz. Bottom: Signal output by the detector after being filtered with a 6th order moving average filter. The sampling rate was 100 MHz.

computationally expensive, and results in a greater amplitude difference between the high and low states. However, isolating the subcarrier with a BPF reduces the receiver's reliance on the AM detectors resolution.

3.3 Undersampling and Digital Filtering

After using the oscilloscope to gain an understanding of the signal created by the NFC system, the STM32 board's in built ADC was used to undersample the carrier signal by a factor of 13. This causes analogue frequencies to be mapped to digital frequencies below the Nyquist sampling rate. Table 3.3 lists the key analogue frequencies and their corresponding digital frequencies. The upper sideband and the 1st harmonic of the carrier signal map to digital frequencies separated by less than 1% of the sampling rate. If the upper sideband was to be isolated then an analogue low pass filter would be required to remove the 1st harmonic. However, since the lower sideband could be isolated with minimal interference, the upper sideband was ignored in this project, removing the need for an anti-aliasing filter.

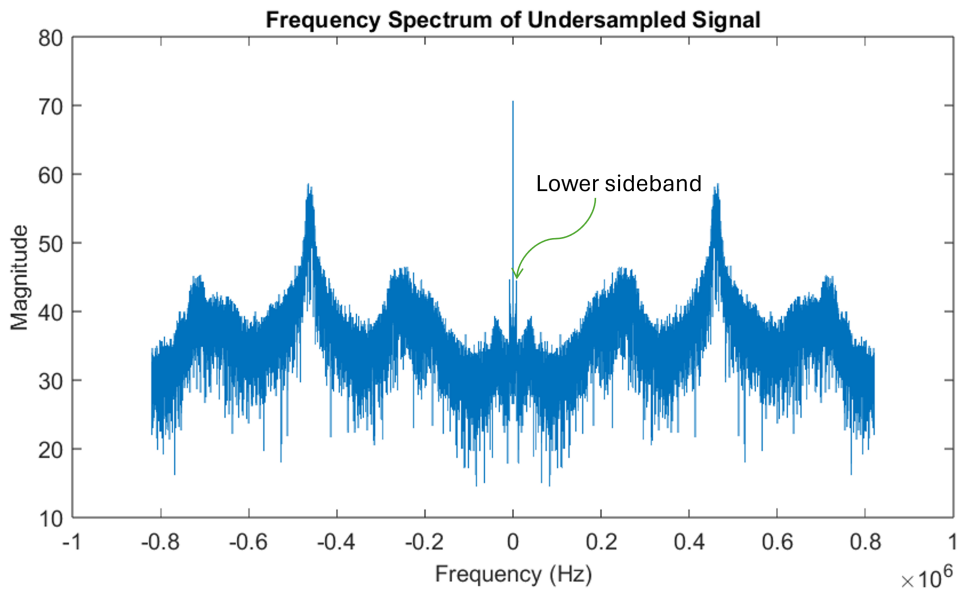


Figure 3.8: Frequency spectrum of the signal output from a notch filter and sampled using the STM32 board.

analogue Frequency (MHz)	Digital Frequency (kHz)
0.423 (subcarrier)	423
13.14 (lower sideband)	20
13.99 (upper sideband)	770
13.56 (carrier)	440
27.12 (1 st harmonic)	760
27.12 (2 nd harmonic)	320

Figure 3.8 shows the frequency spectrum of the signal output from the notch filter after being sampled by the STM32 board. The signal had been passed through an analogue notch filter with a center frequency of 13.56 MHz. Since the 13.99 MHz sideband cannot be isolated, only the 13.14 MHz sideband is relevant, and thus is highlighted in Figure 3.8. After sampling, the lower sideband is the smallest of the major frequency components, at 20 kHz, allowing it to be isolated with a low pass filter.

The carrier signal is 15 dB stronger than the 20 kHz sideband, therefore, the low pass filter must have a low stopband gain to ensure the carrier is completely removed. A small passband ripple is also desirable, as this will prevent any attenuation of the desired frequency component. Figure 3.8 shows that there are no significant peaks near the 20 kHz sideband, making the low pass filters transition bandwidth less critical. Butterworth and Inverse Chebyshev filters meet these criteria, they are maximally flat in the passband, and reach low stopband values. Figure 3.9 compares the

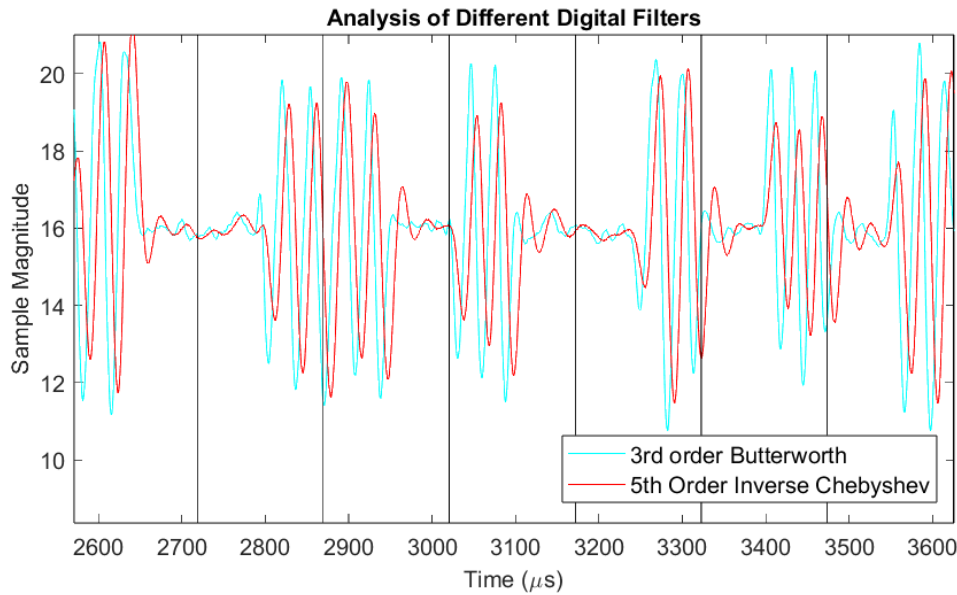


Figure 3.9: The signal output by the coupler after being filtered with a 3rd order butterworth filter alongside the same signal after filtering with a 5th order inverse Chebyshev filter. Sampling was conducted by the STM32 board.

signal output from the coupler after filtering with a 3rd order Butterworth filter and a 5th order Inverse Chebyshev filter. The Butterworth filter requires a lower order, has a faster settling time, and has a larger amplitude difference between the modulated and unmodulated sections, making it the superior choice when digitally filtering this signal.

Figure 3.10 shows the output from the AM detector sampled by the STM32 board, both with and without digital filtering. A 6th order moving average filter was selected due to its low computational complexity and fast response time. When the VICC and VCD are separated by 10 cm, digital filtering increases the Signal to Noise Ratio (SNR) from 3.52 dB to 13.1 dB. Due to the increase in SNR, and the more ideal square wave that is created, Figure 3.10 indicates that digital filtering the signal output by the AM detector will result in a lower BER when demodulating the transmitted message. However, as a square wave is still present without filtering, digital filtering is not essential. This is not the case without the AM detector, as then the digital filtering completely changes the signal.

3.4 Working Principles of The Designed Receivers

When designing the different types of receivers, the aim was to minimise the BER while allowing a large separation between the VICC and VCD. The receiver had limited processing time as it must

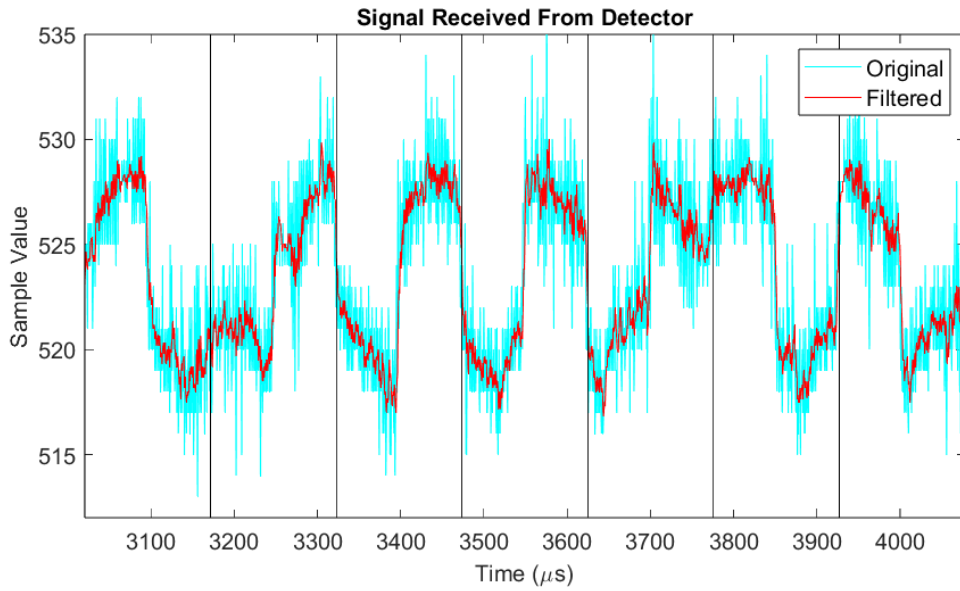


Figure 3.10: The signal received from the detector is plotted alongside the same signal after it has been filtered by a 6th order moving average filter. Sampling was conducted by the STM32 board.

adhere to the strict timing requirements of the ISO 15693 standard, making computational complexity a critical concern. Figure 3.11 shows a high level flowchart outlining the general behaviour of all receivers implemented in this project. The ISO 15693 standard uses Manchester coding, where a logic 0 is represented by modulation in the first half of the bit period, and a logic 1 is represented by modulation in the second half. Therefore, the receivers used in this project assign a score for the samples in the first half of the bit period, and another score for the samples in the second half of the bit period. The scores are calculated based on how likely that section is to have been modulated, allowing an estimate to be made of which half of the bit period modulation most likely occurred in.

In accordance with the ISO 15693 standard, the VICC must respond to a request from the VCD between $318.6 \mu s$ and $323.3 \mu s$ after receiving the VCD's EOF. This leaves a $5 \mu s$ window of uncertainty, which could be reduced if an algorithm is implemented to determine the precise start time of the SOF. The SOF transmitted by the VICC begins with a $56.64 \mu s$ unmodulated section, resulting in the shortest time period between transmission of the VCD's EOF, and the first section of load modulation to be $375.24 \mu s$. The average sample value in this unmodulated section was calculated, and scaled with a value of 1.05 to provide a threshold. The first sample received over this threshold was determined to be the first load modulated sample. This allows precise synchronisation between the VCD and the VICC.

The response by the VICC does not have a consistent length, therefore, an EOF is used to

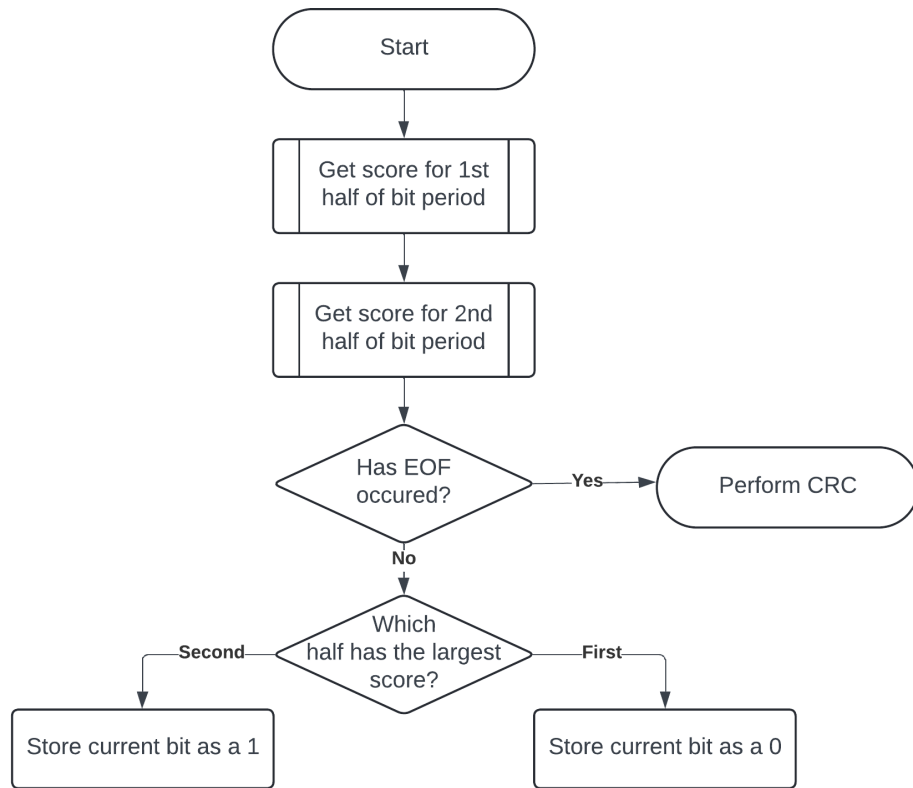


Figure 3.11: Flowchart which shows the general behaviour of all implemented receivers.

inform the VCD that the message has finished. Consequently, at each bit period a function must be applied to estimate if the EOF has been transmitted. The EOF begins with the signal for a logic 0, followed by $56.64 \mu s$ of modulation and then $56.64 \mu s$ of no modulation. In all the receivers, the signal is divided into $37.76 \mu s$ bit periods, and scores are defined for each half of the bit period. Figure 3.12 shows the EOF when it has been split into sections of length equal to the bit period. The EOF begins with a logic 0, then an entirely modulated section, another logic 0, and finally an entirely unmodulated section. Neither an entirely modulated, nor an entirely unmodulated bit period will occur elsewhere during the response. As a result, the scores calculated by the receivers for each half of the bit period can be used to determine if the EOF has been transmitted. The difference in scores between the entirely modulated and entirely unmodulated sections should be substantially larger than the difference in scores observed elsewhere in the message, where each bit period is always half modulated. Therefore, at each bit period, the difference between the current scores and the scores from two bit periods past was calculated, normalised and then compared with a threshold value to determine if the EOF has occurred. To further reduce errors, it was ensured that the entirely modulated section was both preceded and succeeded by a logic 0. For applications where a high SNR is expected, and computational complexity is crucial, a second method of estimating if the EOF has been transmitted was implemented. This method detects

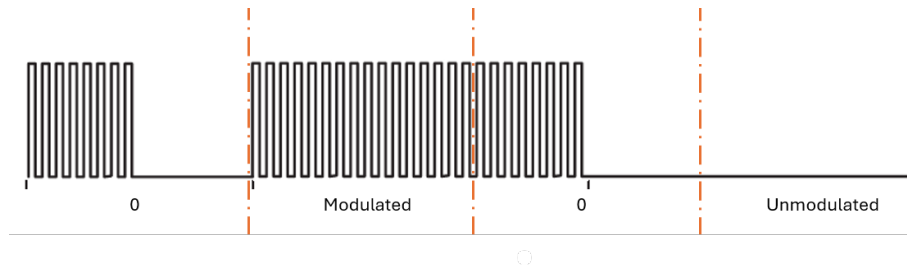


Figure 3.12: The EOF transmitted by the VICC, broken down into windows the size of a bit period

when a logic 1 is followed by an entirely modulated section, and ignores the subsequent $94.4 \mu s$ of the EOF. This allows the processor to use the $94.4 \mu s$ as additional processing time, increasing the computational efficiency of the algorithm, but resulting in a higher likelihood that a wrong decision will be made.

The first receiver designed used thresholding in combination with an AM detector. The SOF transmitted by the VICC contains $56.64 \mu s$ of modulation and $56.64 \mu s$ of no modulation. Therefore, an average value for the amplitude of the signal in the modulated and unmodulated sections was calculated, allowing a 50% threshold value to be implemented. Figure 3.13 shows a flowchart that describes how the threshold receiver calculates the score for the first and second halves of the bit period. The parameter X can be adjusted depending on the required computational efficiency. The maximum value of X corresponds to the number of samples in half a bit period, this provides the largest accuracy but requires the highest processing time. Each sample is compared to the threshold, if it exceeds the threshold, then the sample is classified as modulated and the score is incremented by one. Therefore, when the two scores are compared, the highest score arises from the section with the largest number of samples over the threshold.

To enhance the VCD's performance, a correlation receiver was implemented alongside the AM detector. Figure 3.14 shows the subcarrier load modulation performed by the VICC during the transmission of a logic 1. Cross-correlating the received signal with the true modulation sequence shown in black in Figure 3.14 yields the highest correlation score. However, the square wave has a frequency of 423 kHz, which is only three times lower than the sampling rate, resulting in each pulse being represented by three samples after digitization. Consequently, if the VCD is misaligned with the true bit period by one sample, the message cannot be decoded. To address this issue, the square wave depicted by the dashed green line in Figure 3.14 was cross-correlated with the received signal. Each pulse is now represented by thirty samples, reducing the receiver's dependence on synchronisation between the VCD and the VICC. To prevent a relative decrease in the correlation score, only the largest sample in a three sample window was used for the correlation.

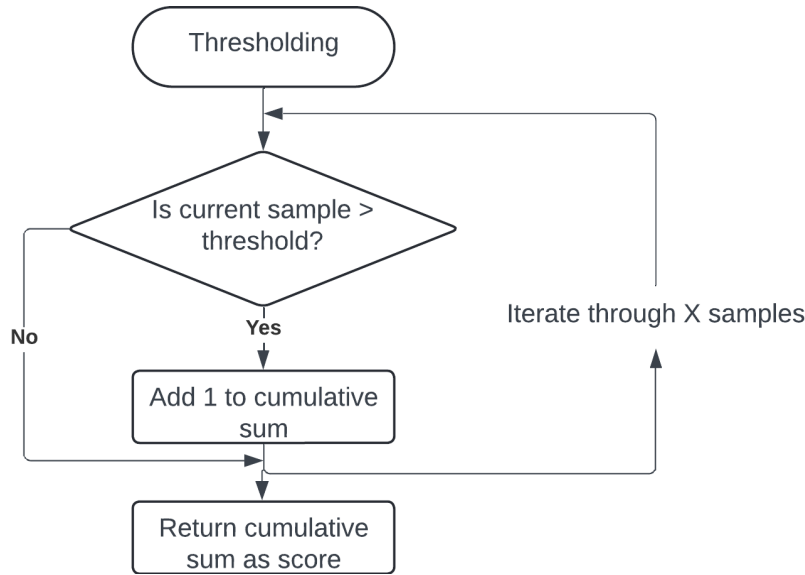


Figure 3.13: Flow chart followed when implementing a threshold receiver to work alongside an AM detector.

This ensures that only samples where the square wave is logic high are used in the correlation, as in the modulated half of a bit period, a three sample window will always contain at least one sample where load modulation has been applied. Although this method is more susceptible to noise, the reduced reliance on synchronisation was found to improve the receiver's performance, when compared with correlating directly with the true square wave.

The cross-correlation between two signals was calculated in this project using the formula $r_{xy} = \sum_{n=0}^N x[n]y[n]$, where x represents the received signal, y is the ideal signal, and N denotes the number of samples in a bit period. For each bit period, two cross-correlations are performed, one with the ideal signal corresponding to a logic 1, and another with the ideal signal for a logic 0. The cross-correlation that results in the highest value of r_{xy} indicates the greatest similarity between signals, and therefore identifies the most likely bit transmitted by the VICC. The ideal signal is a square wave with a high value of one, and a low value of zero. Consequently, half of the bit period is always multiplied by zero, and thus can be excluded from the summation, greatly reducing the computational cost of the algorithm. The other half of the bit period multiplies the signal by one, allowing the computational cost to be further reduced by removing all multiplications. This allows two new formulas to be derived that require no multiplications, and only $N/2$ additions. Cross-correlating the received signal with the expected message for a logic 0 simplifies to Equation 3.4.1, while cross-correlating with the ideal signal for a logic 1 simplifies to Equation 3.4.2. The receiver created using these algorithms was designed following the flow chart in Figure 3.15.

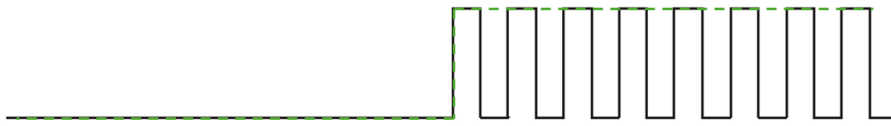


Figure 3.14: Subcarrier load modulation sequence performed by the VICC when transmitting a logic 1. The Dashed green line shows the signal used for cross-correlation.

3

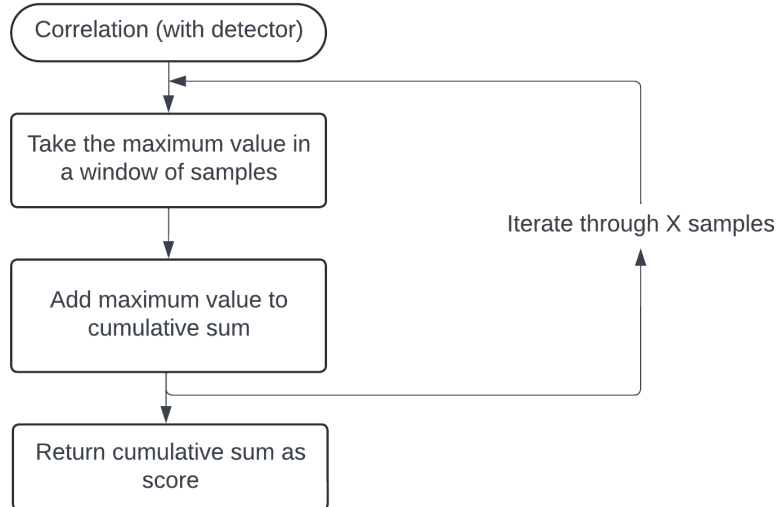


Figure 3.15: Flow chart followed when implementing a correlation receiver to work alongside an AM detector

$$r_{x0} = \sum_{n=0}^{N/2} x[n] \quad (3.4.1)$$

$$r_{x1} = \sum_{n=N/2+1}^N x[n] \quad (3.4.2)$$

Receivers were also designed to perform the entire detection process digitally, eliminating the need for an AM detector. Figure 3.9 shows that after the signal has been undersampled, the subcarrier information is contained within a 20 kHz sine wave. Therefore, when a low pass filter is applied to isolate this frequency component, a larger amplitude is expected during the modulated half of a bit period. Two methods were implemented to calculate the average amplitude in each half of the bit period.

The first method calculates the maximum and minimum values within a window of samples, then determines the difference between these values to provide an estimate of the peak amplitude. The window length was chosen to correspond to half the period of the sine wave, ensuring at least one maximum or minimum value is captured. This window length allows the average amplitude within three windows to be calculated, providing a robust estimate for the signal amplitude. The

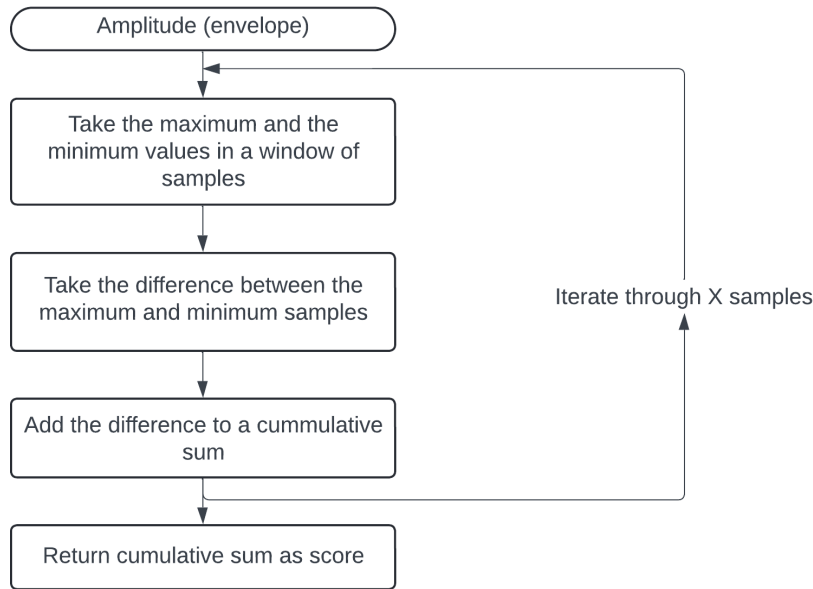


Figure 3.16: Flow chart followed when implementing an amplitude receiver. Method 1

flowchart in Figure 3.16 was followed when implementing a receiver based on this method of determining the signals amplitude.

The second method for determining the average amplitude within half a bit period was created following the flow chart in Figure 3.17. Here, the first order time derivative is calculated in order to identify the locations of the signal's maxima and minima. When a change in sign of the gradient is detected, the difference is calculated between the current sample value and the sample value from the previous sign change. This difference is added to a cumulative sum. Once all the samples have been iterated through, the cumulative sum is divided by the total number of sign changes detected, providing an estimate for the peak-peak amplitude of the signal. This method required additional digital filtering to prevent the gradient changing sign due to noise.

In addition to the two amplitude receivers, a correlation receiver was implemented without the AM detector. Figure 3.18 shows the flow chart followed when determining the score for each half of the bit period. This receiver uses Equations 3.4.1 and 3.4.2 to calculate the correlation scores for a logic 0 and logic 1 respectively. As with the first amplitude receiver, the maximum and minimum values within a window are calculated. However, instead of computing the difference, these values are added to separate correlation score summations, providing a minimum correlation score and a maximum correlation score. Modulation increases the high correlation score and decreases the low correlation score, but in low SNR environments, only one of these changes might occur. Therefore, utilising both scores increases the receiver's robustness to noise. The difference between the low

3

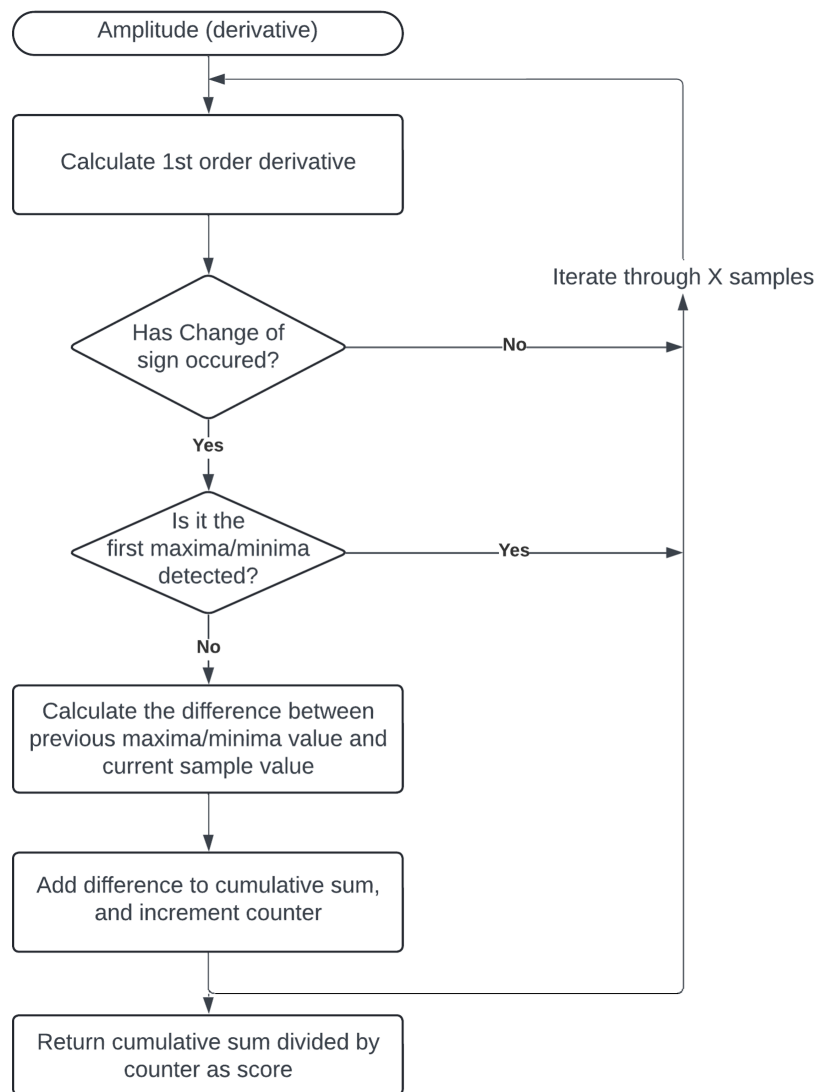


Figure 3.17: Flow chart followed when implementing an amplitude receiver. Method 2

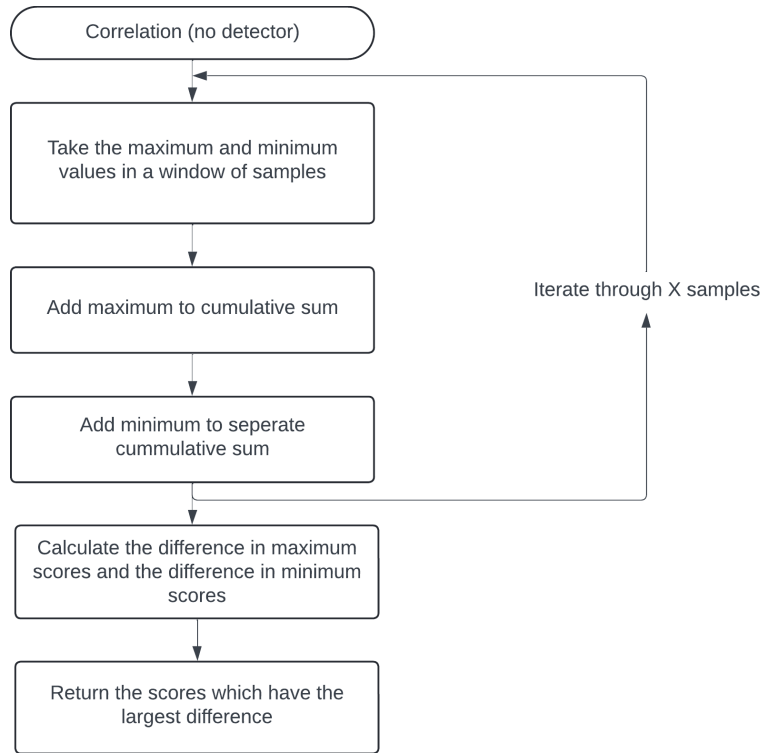


Figure 3.18: Flow chart followed when implementing a correlation receiver to work without an AM detector.

correlation scores for the two halves of the bit period is calculated, as well as the difference between the high correlation scores. The correlation scores that produce the largest difference are selected to represent the system.

3.5 Results and Analysis

For the initial analysis and testing, the receiver designs discussed above were implemented in MATLAB. Once each receiver was capable of resolving the VICC's UID, the receivers were implemented in C and loaded onto the STM32 board. A function was formed to send 1000 requests to the VICC at 20ms intervals. For each request, the response from the VICC was demodulated using a receiver and compared with the true message, allowing an average BER to be formed for each receiver design.

Figure 3.19 presents the BER as a function of the distance between the VICC and VCD when no AM detector is used. "Amplitude (gradient)" refers to the method of determining the average amplitude by finding the locations where a change of sign occurs in the signals gradient. This approach results in the highest BER across all distances. The "Amplitude (difference)" method

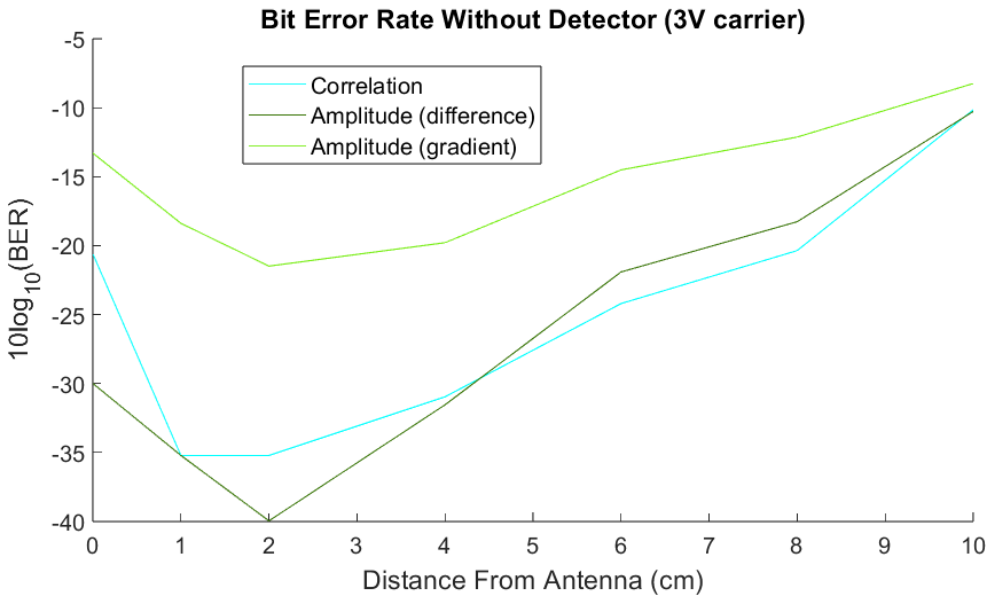


Figure 3.19: BER as a function of the distance between the VICC and VCD for different methods of reception. The carrier wave had an amplitude of 3V and no AM detector was used

estimates the amplitude as the difference between the maximum and minimum values within a predefined window. While this method provides the lowest BER at short read ranges, the correlation receiver results in a lower BER at distances greater than 4 cm. At large read ranges, where the SNR is low, the sine wave which occurs in the modulated section is heavily distorted, reducing the amplitude difference between the modulated and unmodulated sections. This results in the amplitude based receivers being ineffective at large read ranges. Correlation on the other hand is inherently noise resistant, since the important factor is the average value in each half of the bit period. The computational complexity of these algorithms are the same, with the processing time being dominated by the two decisions that have to be made with each sample.

Figure 3.20 shows the BER as a function of the distance between the VICC and VCD when an AM detector is used to assist with signal demodulation. At distances where the signal is not visible, no errors were recorded, causing the logarithmic BER to tend towards negative infinity. A BER of 0.5 was observed when the VICC was in contact with the VCD, introducing a minimum read range that was not present without the AM detector.

When using the correlation receiver at distances in the range 1-8 cm, digital filtering provides more consistent performance. However, for read ranges over 8cm, the un-filtered signal results in a lower BER. This highlights the importance of considering the expected read range before implementing digital filtering. The thresholding system has a lower BER at all distances when digital filtering is applied. If a BER of 1% is considered the cutoff for acceptable performance,

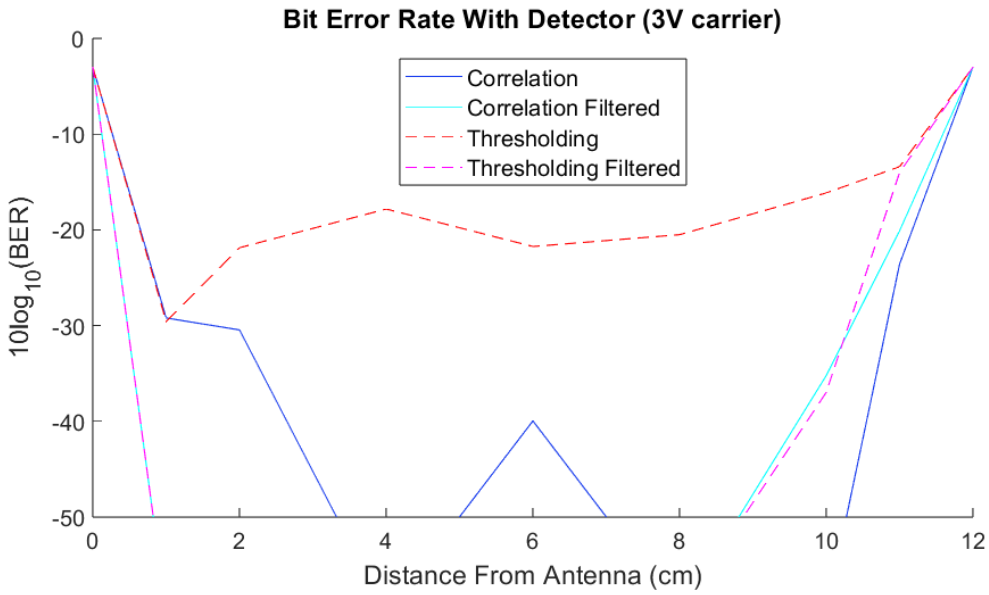


Figure 3.20: BER as a function of the distance between the VICC and VCD for different methods of reception. The carrier wave had an amplitude of 3V and an AM detector was used

the correlation receiver provides an additional 1 cm of read range when compared to the threshold receiver. A comparison between Figures 3.20 and 3.19 shows that using an AM detector results in a lower BER for all distances greater than 1cm, however, the signal cannot be demodulated for read ranges less than 1cm.

The computational complexity of the threshold and correlation receivers are the same, with a single decision being made for each sample. This is half the number of decisions required when no AM detector is used. Therefore, implementing an analog AM detector results in a longer read range and reduces the processing time.

In order to extend the read range, the amplitude of the carrier wave was increased from 3V to 5V. This voltage increase raised the antenna's transmitted power from 0.09 W to 0.25 W. Figure 3.21 shows the BER for various read ranges when the correlation receiver was used alongside an AM detector to decode the signal. Due to an increase in noise, digital filtering now results in a lower BER for all distances greater than 2 cm, when compared to processing the unfiltered signal. The increase in transmission power extended the maximum reliable read range from 11 cm to 14 cm, but it also increased the minimum readable distance from 1 cm to 2 cm. To prevent the VICC from entering this minimum read range, a casing could be designed to maintain a 2 cm gap between the surface of the VCD and its antenna. However, this would effectively reduce the receiver's read range by 2 cm.

In the previous experiments, the '1 out of 4' coding mode of the ISO 15693 standard was used.

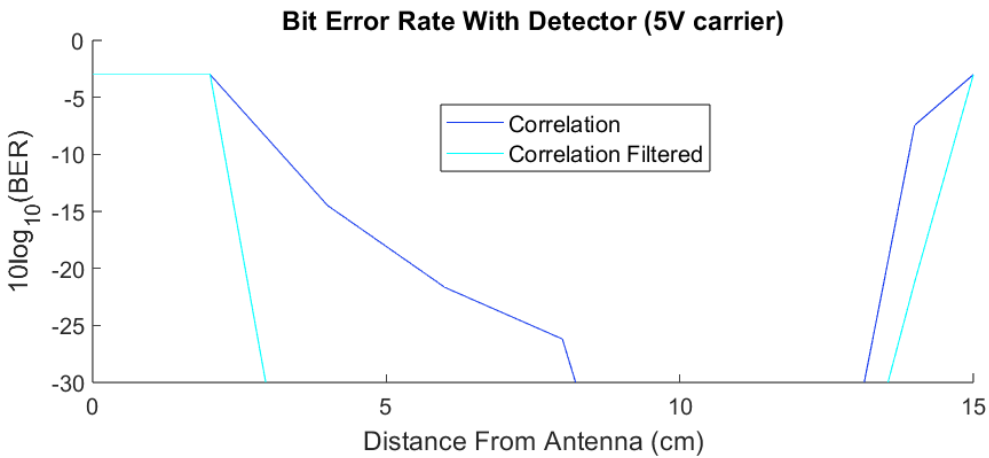


Figure 3.21: BER as a function of the distance between the VICC and VCD for the correlation receiver. An AM detector is employed and the carrier wave has an amplitude of 5V.

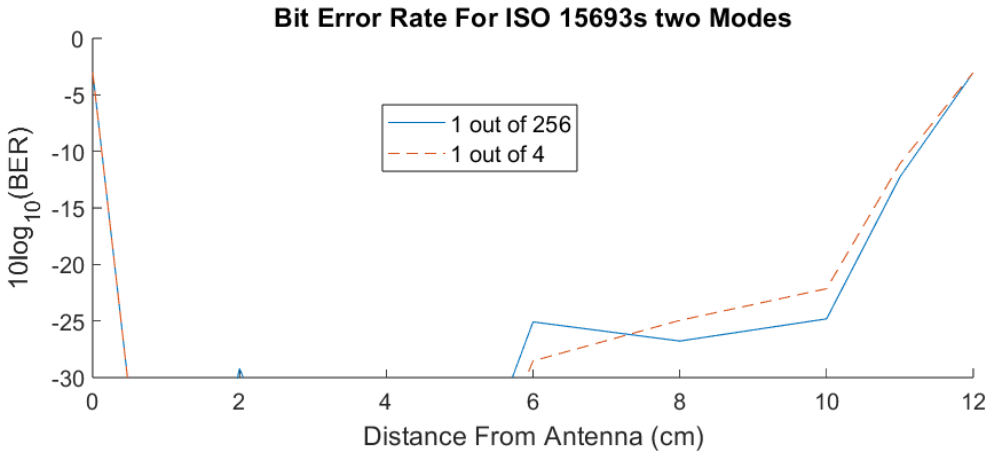


Figure 3.22: BER as a function of distance between the VICC and VCD when a correlation receiver is used. Both the '1 out of 4' and '1 out of 256' transmission modes are plotted

This mode has a faster data rate when compared to the '1 out of 256' coding mode, but transmits less power to the VICC. Therefore, it is expected that the '1 out of 256' mode would have a larger read range. Figure 3.22 shows the BER for both '1 out of 256' and '1 out of 4' coding modes when a correlation receiver is used for demodulation. While the '1 out of 256' coding mode results in a reduced BER at distances between 8 and 11cm, it imposes stricter timing requirements, and due to a jitter in the transmission time of the message, 4.8% of the requests did not yield a response from the VICC. To ensure that the VICC consistently responds to a request when in the '1 out of 256' mode, the STM32 board would have to be replaced with a microcontroller that has a higher timing resolution, increasing the system cost.

4

Localisation

Contents

4.1 Hardware and Received Signals	33
4.2 Localisation Techniques	36
4.3 Results and Analysis	38

4.1 Hardware and Received Signals

When estimating the location of the VICC, the antenna consisting of a single loop which was used in Chapter 2, was replaced with the two dimensional travelling wave antenna shown in Figure 4.1. This antenna consists of nine loops, each spaced 20 cm apart. Both ends of the antenna provide an output that can be read by the VCD. After the VICC modulates the carrier wave, the transmitted and reflected signals travel a different distance within the antenna before reaching their respective outputs. The difference in distance travelled by the two signals depends on which loop is closest to the VICC. This allowed the VICC's location to be estimated using the TDOA between the two outputs of the antenna.

An AM detector was used at each output, creating a square wave that was filtered to provide a clear transition point where the signals move from unmodulated to modulated. The block diagram in Figure 4.2 shows the hardware setup used in the laboratory for estimating the location of the VICC. The localisation system was first designed in MATLAB to process data collected from the digital oscilloscope. The project was then completed by implementing the localisation system on

4

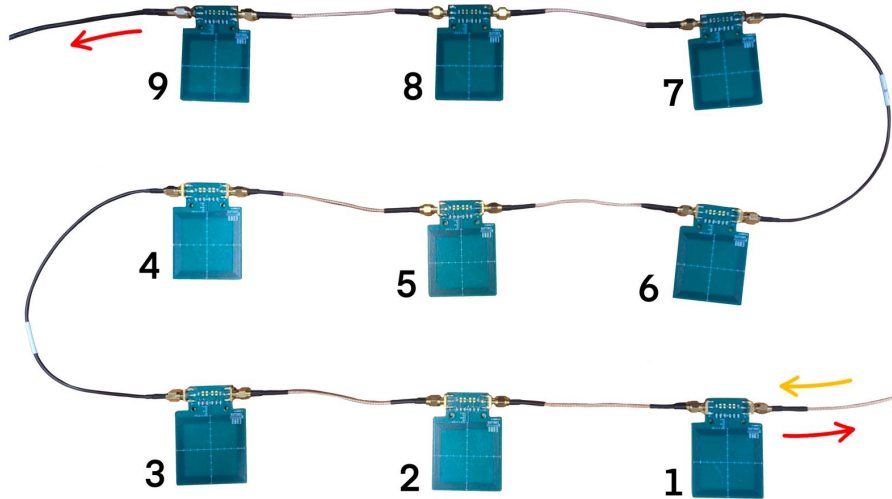


Figure 4.1: Picture of the travelling wave antenna which was used for VICC localisation. The red arrows indicate the outputs, while the yellow arrow shows the input.

to the STM32 board.

The signal received from each AM detector when the VICC was positioned 1 cm from loop 1 can be seen in Figure 4.3, where 'Output 1' is the transmitted signal read directly from the antenna, while 'Output 2' is the reflected signal read from the coupler. To improve the consistency of the localisation systems, a low pass digital filter was applied to smooth the signal. In this project different sampling rates were tested, therefore, different order filters were required, table 4.1 shows the order of the filter implemented at each sampling rate.

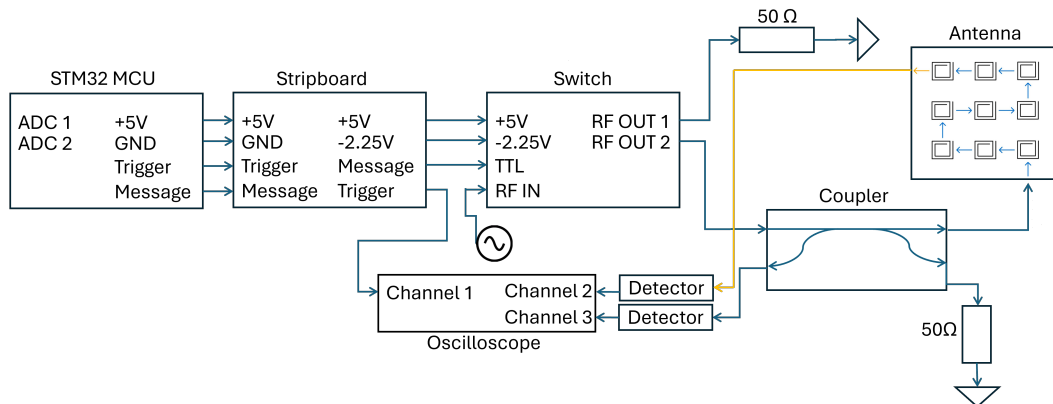


Figure 4.2: Block diagram of the hardware used when estimating the location of a VICC

Sampling Rate (MHz)	1	2	4	5	10	20	25	50	100
Filter Order	3	3	3	3	5	7	7	7	10

Table 4.1: The order of the moving average filter applied to both outputs of the travelling wave antenna for different sampling rates.

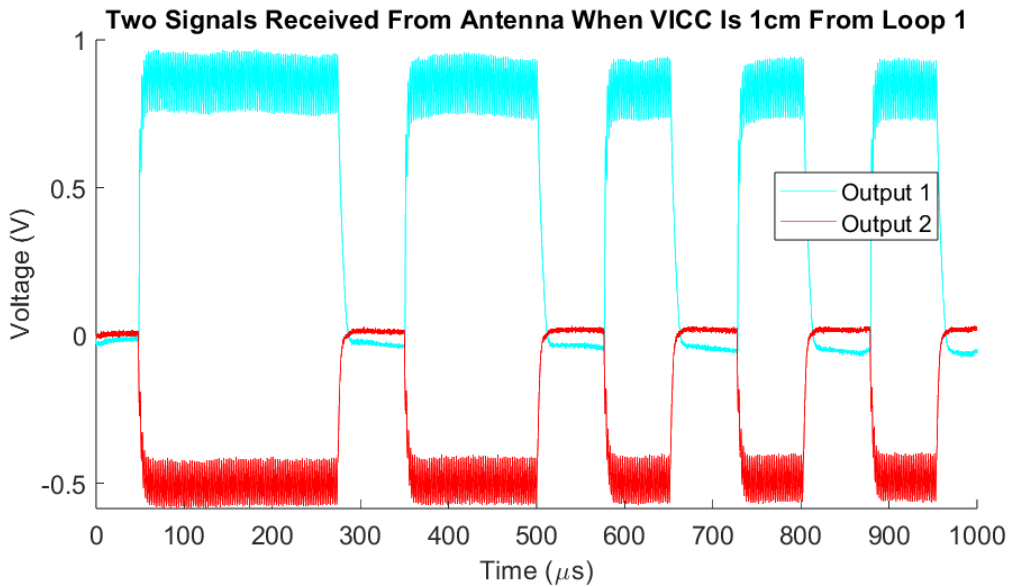


Figure 4.3: The signals read from both outputs of the antenna, sampled by the oscilloscope when operating at 100 MHz.

The top plot of Figure 4.4 shows the first corner of the square wave received when the VICC is positioned at loop 1, while the bottom plot shows the same section of the signal but when the VICC is positioned at loop 9. The TDOA changes from $-0.72 \mu s$ at loop 1 to $0.7 \mu s$ at loop 9. Assuming the travelling wave has a constant group velocity through the antenna, the expected change in TDOA between adjacent loops is $0.18 \mu s$. Therefore, the minimum sampling rate required to differentiate between all loops is 5.6 MHz. 'Output 1', which is measured directly from the antenna, has a steeper transition gradient when compared to 'Output 2', which is read from the coupler. This difference in transition gradient was found to affect the TDOA measured using thresholding.

The sampling rate is an important consideration when implementing a digital electronic system. Higher sampling rates more accurately represent the original signal, but require a larger data rate, consume more power, and incur higher manufacturing costs. Therefore, it is important to tailor the sampling rate to the application, keeping it as low as possible, while ensuring a high degree of accuracy. For this reason an analysis was conducted on the classification error at different sampling rates. Sampling rates of 1, 2, 4, 5, 10, 20, 25, 50 and 100 MHz were tested to provide an overview of which sampling rate would be optimum for different applications.

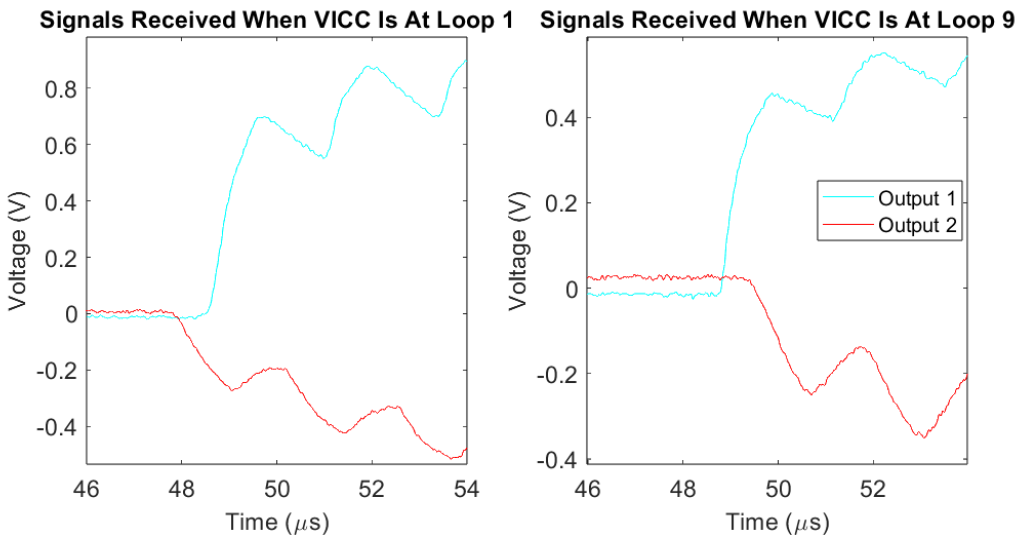


Figure 4.4: The first state transition of the square waves output from the AM detectors. The signals were sampled at 100 MHz and filtered with a digital moving average filter.

4.2 Localisation Techniques

A jitter of $0.5 \mu s$ in the response time of the VICC was unavoidable, leading to $0.5 \mu s$ of uncertainty in all TOA measurements. Since the TOA changes by $0.18 \mu s$ on average between neighbouring loops, a single TOA measurement can not be used to accurately locate a VICC. In contrast, the TDOA is unaffected by this jitter. Since both antenna outputs are effected by the same jitter, calculating the difference between the measured TOAs cancels out the jitter.

The in built ADC of the STM32 board has a sampling period of $0.61 \mu s$. The average change in TDOA between adjacent loops is $0.18 \mu s$, necessitating a gap of four loops before the STM32 board can detect a change in the TDOA. Consequently, only loops 1, 5, and 9 could be effectively classified. Even when using three loops, there is only a single sample difference in the TDOA between adjacent loops, requiring the system to be accurate to the nearest sample for each measurement.

Two methods were implemented to estimate the TDOA. The first method calculates the TDOA using Equation 4.2.1, where S_{out1} is the index of the first modulated sample of 'Output 1', S_{out2} is the index of the first modulated sample of 'Output 2', and T_s is the sampling period. A threshold detector was used to identify the first modulated sample for both antenna outputs. This method has a low computational cost but requires selecting a threshold, the value of which will affect the measured TDOA.

$$TDOA = (S_{out1} - S_{out2})T_s \quad (4.2.1)$$

The VICC's SOF was used to calculate the threshold before any bits were transmitted. After the VCD transmits it's EOF, there is an unmodulated section of length $375.24 \mu s$, followed by a modulated section of length $56.64 \mu s$. The average value of each section was calculated, providing a modulated and unmodulated average. These averages were then used to determine a 10 % threshold. A 10 % threshold was used to mitigate the effect of 'Output 1' and 'Output 2' having different gradients when transitioning between the high and low states. The same threshold was used for both signals. 'Output 2' was used to calculate the threshold as this signal had a smaller absolute amplitude than 'Output 1'. The SOF finishes with the code sequence for a 1, therefore, the state transition which occurs here can be used to estimate each signals TOA. This means that the entire localisation system can be conducted before the first bit of the VICC's message is transmitted.

The second method implemented to find the TDOA uses cross-correlation to directly estimate the delay between the two outputs. Equation 4.2.2 shows how cross-correlation is applied to estimate the TDOA, where s represents the delay in samples, x_1 and x_2 are the antenna output signals, and T_s is the sampling period. The computational complexity can be reduced by limiting the range of sample delays, s , which are tested. Since the TDOA should not go over $1 \mu s$, the values of s can be limited to $\pm 1 \times 10^{-6} \times f_s$, where f_s is the sampling rate. The maximum value of N is the total number of samples in the response, yielding the most accurate TDOA but also the highest computational cost. To further increase the algorithms efficiency, N was chosen to encompass only nine state transitions, minimising the computational cost with negligible impact on the measured TDOA. Despite these methods of limiting the computational cost, cross-correlation still requires substantially more processing time than the thresholding method.

$$TDOA = \arg \max_s \left[\sum_{n=0}^N x_1[n+s]x_2[n] \right] T_s \quad (4.2.2)$$

If each loop of the travelling wave antenna is thought of as a class, then the localisation system becomes a classification system, where the aim is to assign the measured TDOA to a loop. Training data was used in MATLAB to create a decision tree that assigns each loop a region. The decision tree was then applied to test data, allowing a confusion matrix to be formed which identified the locations of all errors. In classification systems Fisher's Discriminant Ratio (FDR) provides a

measure of how easily classes can be separated, and is calculated using equation 4.2.3 [39], where μ_1 and μ_2 are the means of the classes being compared, and σ_1^2 and σ_2^2 are the variances of the classes. FDR was calculated for both thresholding and cross-correlation systems to provide a measure of their robustness.

$$FDR = \frac{(\mu_1 - \mu_2)^2}{(\sigma_1^2 + \sigma_2^2)} \quad (4.2.3)$$

4.3 Results and Analysis

The location of the VICC was estimated by analysing the TDOA from the signals detected at both ends of a travelling wave antenna. Initially, data was collected using a digital oscilloscope and processed in MATLAB. Once this was completed, the entire localisation system was implemented on the STM32 board. Two methods were used to determine the TDOA: thresholding and cross-correlation. A classification system was designed by training a decision tree to assign a TDOA measurement to a loop.

Figure 4.5 shows 100 TDOA measurements taken at each loop, plotted against the loop number the data was collected at. The data is linearly correlated, showing that classification based on this data is possible using a single feature decision tree. To ensure the classification systems are accurate within the entire read range, when collecting the data presented in Figure 4.5, the VICC was moved between each measurement. The centre of the VICC could be moved out of alignment with the centre of a loop by 3 cm in any direction before the localisation systems began to produce inconsistent measurements. The message transmitted by the VICC could still be demodulated when the VICC was outside of this range, indicating that the localisation systems are less robust to noise than the receivers designed in Chapter 3.

It is not possible to separate the x-axis of Figure 4.5 into nine regions that each exclusively contain the data from a single loop, preventing a classification system from reaching 100% accuracy. However, as the VICC moves from loop 1 to loop 9, the TDOA decreases, forming a pattern that can be exploited to classify the TDOA values into specific loops. Table 4.2 shows the mean TDOA measured at each loop, further highlighting how the TDOA decreases as the VICC moves from loop 1 to loop 9. Both thresholding and cross-correlation have two instances where a change in loop results in an increase in the mean TDOA instead of a decrease, indicating that when measuring a TDOA, factors other than the distance travelled have influenced the recorded value. It was

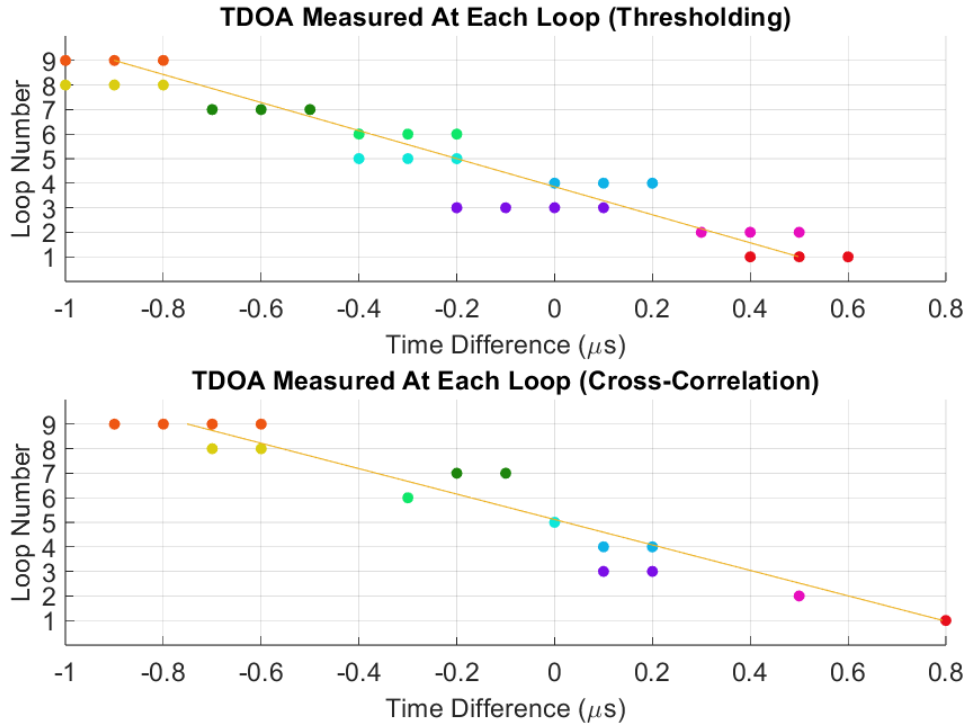


Figure 4.5: TDOA measured at each loop plotted against the loop number it was measured at. Top: TDOA measurements made using thresholding. Bottom: TDOA measurements made using cross-correlation. The signal was sampled at 10 MHz.

	Loop 1	Loop 2	Loop 3	Loop 4	Loop 5	loop 6	loop 7	loop 8	loop 9
Thresholding (μs)	0.509	0.358	0.008	0.066	-0.267	-0.302	-0.557	-0.968	-0.910
Cross-Correlation (μs)	0.799	0.495	0.099	0.199	0	-0.299	-0.149	-0.599	-0.799

Table 4.2: Mean TDOA at each loop, measured using both thresholding and cross-correlation. 100 measurements were taken at each loop using a digital oscilloscope operating at 10 MHz.

predicted that when moving to a neighbouring loop, the change in TDOA would be consistent, irrelevant to which was the original loop. However, Table 4.2 shows that there is a large variation in how much the TDOA changes between neighbouring loops. This lead to some loops being easier to separate from their neighbours than others.

The TDOA measurements were separated into training and test data using a ratio of 60:40. The training data was used to develop a model for the localisation system by training a single decision tree. The thresholding and cross-correlation data was always kept separate and used to train different models. The test data was applied to the decision tree for loop classification, with the results from this classification presented in the confusion matrices in Figure 4.6. The cross-correlation system has an average error rate of 3.06% and can identify all but the third and fourth loops with 100% accuracy. The threshold system on the other hand, was unable to identify any

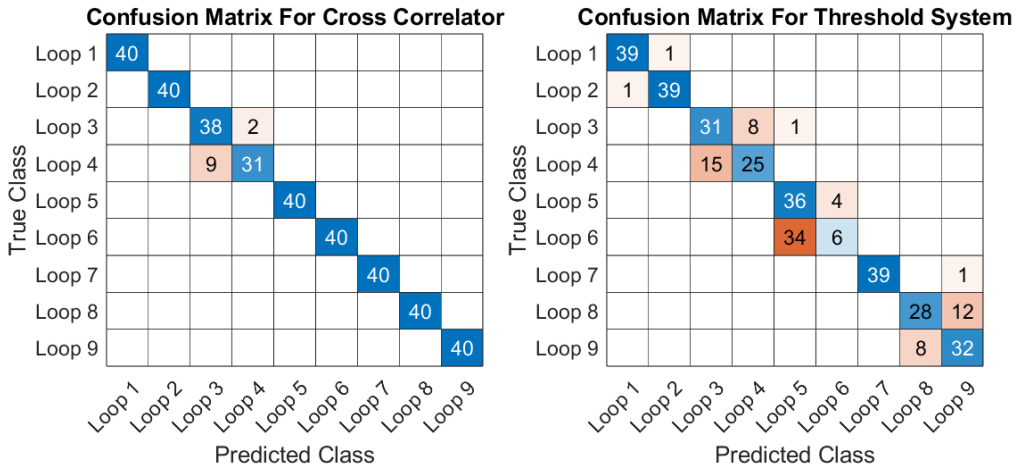


Figure 4.6: Confusion matrices for cross-correlation and thresholding systems when attempting to classify a TDOA into 1 of 9 loops. The signal was sampled at 10 MHz

loop with 100% accuracy, and has an average error rate of 34.2%. Therefore, if thresholding is to result in consistent performance, either the number of loops must be reduced, or the sampling rate increased.

Figure 4.7 shows how the error rate in test data classification changes when the sampling rate increases, for both thresholding and cross-correlation systems. For the cross-correlation system, the error rate reaches its minimum value of 3% at a sampling rate of 10 MHz. The cross-correlation error rate increases to 40% when the sampling rate decreases to 5 MHz. This makes 10 MHz the most pragmatic choice of sampling rate for many applications where the sampling rate is limited. Even with a sampling rate of 100 MHz, the error rate for the thresholding system never goes under 11%, therefore, fewer loops are needed for reliable classification.

A 5-class classification system was created by taking the TDOA measurements from every second loop, and a 3-class classification system was created by taking the TDOA measurements from every fourth loop. The unused loops were not removed as this would increase the group velocity of the MI wave, reducing the difference in the TDOA between neighbouring loops. Figure 4.8 shows the error rate for these classification systems at different sampling rates. The best performance at low sampling rates is achieved when the TDOA is measured using thresholding and only 3 loops are used. Here, a sampling rate of 2 MHz can be used to reach an error rate of 1%, and the error rate decays to zero for all higher sampling frequencies. When thresholding is used with 5 loops, a sampling rate of 15 MHz is needed before the error rate reaches zero. Cross-correlation outperforms the thresholding system when differentiating between 5 loops, with the error rate reaching zero at 10 MHz. Selecting an appropriate sampling rate is more critical

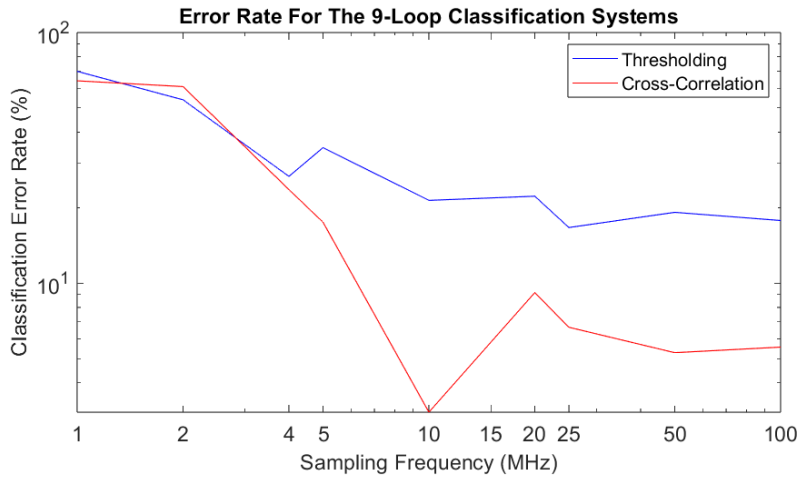


Figure 4.7: Error rate when applying test data to a trained decision tree in order to classify TDOAs to a loop. All nine loops of the travelling wave antenna were used.

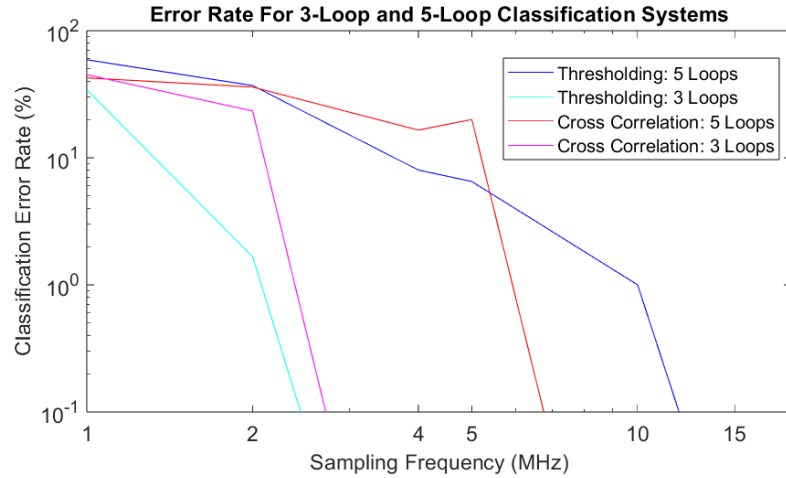


Figure 4.8: Error rate when applying test data to a trained decision tree in order to classify TDOAs to a loop. Two decision trees were tested, one where only the data from 5 loops was used, and the other using only data from 3 loops.

for cross-correlation systems as the computational cost increases quadratically with the number of samples, while the computational cost increases linearly for the thresholding system.

The error rate in classifying data gives no indication of the confidence in each decision, or the robustness of a classification system. This can be obtained by FDR, which provides an indication of how easily two classes can be separated. FDR was calculated between each loop and its two neighbouring loops, the mean FDR was then calculated to provide a single value which represents the system's separability. Figure 4.9 shows how the mean FDR changes as the sampling rate increases. For sampling rates below 4 MHz, the cross-correlation system does not yield an average FDR which truly represents the separability of the system, due to outliers caused by variances close to zero. At sampling rates greater than 5 MHz, FDR increases with the sampling rate for

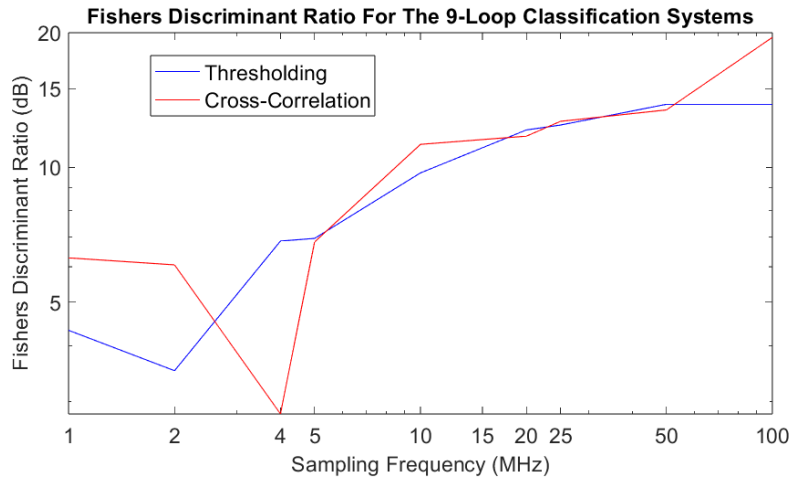


Figure 4.9: Fishers discriminant ratio against the sampling rate when all 9 loops of the antenna are used

both thresholding and cross-correlation systems. The class means were found to remain relatively unchanged, but the variance within a class decreased as the sampling rate increased, leading to the observed increase in FDR. For the cross-correlation system, the error rate in Figure 4.7 indicated that 10 MHz was the optimal sampling rate, however, FDR continues to increase for higher sampling rates. Therefore, while the error rate may not increase, higher sampling rates result in a more robust system. While cross-correlation resulted in a lower error rate when compared to thresholding, there is no clear difference in FDR between the two methods.

Figure 4.10 shows how FDR changes with the sampling rate when 3-class and 5-class classification systems are employed. When the number of loops used from the traveling wave antenna decreases, the distance between neighbouring loops increases, making the TDOAs easier to separate for lower class systems. This is verified in Figure 4.10 as FDR increases when the number of classes is reduced. At low sampling rates, the TDOAs measured using thresholding result in a higher FDR, and as the 3-class system which employed thresholding had the lowest error rate in Figure 4.8, this should be the preferred method when the sampling rate is limited.

Once localisation had been successfully implemented using a combination of a digital oscilloscope and MATLAB, the STM32 board was employed to both sample and process the data. The ADC clock frequency of 1.64 MHz is less than required to accurately differentiate between all nine loops, therefore, a maximum of every other loop was used to test the localisation on the STM32 board. Figure 4.11 shows the normalised frequency polygons for the TDOA measurements at each loop calculated using thresholding. As the VICC moves between loops there is a clear change in the TDOA, however, for many of the transitions there is an overlap, resulting in an area of uncertainty.

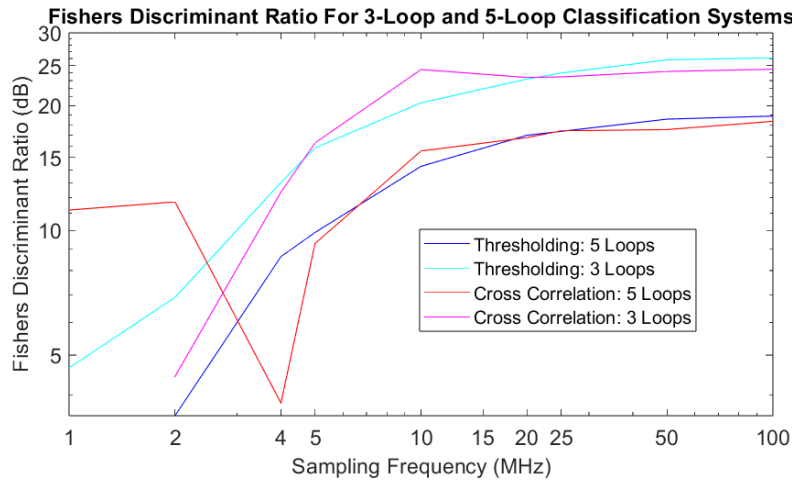


Figure 4.10: Fishers discriminant ratio against the sampling rate when data from only 5 loops, and data from only 3 loops was used to define classes.

Loop 1 and loop 9 have completely separate regions, but both overlap with the region of loop 5, resulting in a maximum of 2 classes for 100% accuracy in classification.

The TDOA measurements were split with the ratio 60:40 into training and test data. A decision tree was created using the training data, and then used to classify the test data. The confusion matrices for the 3-class and 5-class systems can be seen in Figure 4.12. For a 5-class classification system, an error rate of 15.2% occurs, but if a 3-class classification system is trained, then the error rate drops to 0.28%.

Both of these error rates are lower than expected for a sampling frequency of 1.64 MHz. This occurs as a larger range of TDOAs were measured using the STM32 board, when compared with the oscilloscope and MATLAB. When processing the data in MATLAB, a 10% threshold was created, while for the processing conducted on the STM32 board, this threshold was found to result in inconsistent measurements. Therefore, in order to enhance the system's robustness, a 20% threshold was implemented when processing on the STM32 board. This alters the TDOA measured as the two outputs from the travelling wave antenna have different transition gradients. The TDOAs are further influenced as the power of the reflected signal, which is read from the coupler, decreases as the VICC moves from loop 1 to loop 9, causing a corresponding decrease in the transition gradient. If the transition gradient decreases, then the measured TOA increases as it takes longer for the signal to reach the threshold. Although these results were found to be consistent in testing, it leaves the localisation systems performance unpredictable if the environment or hardware changes.

Cross-correlation was also implemented on the STM32 board, Figure 4.13 shows the normalised frequency polygons for the TDOA measurements at loops 1, 5, and 9. There is now a maximum

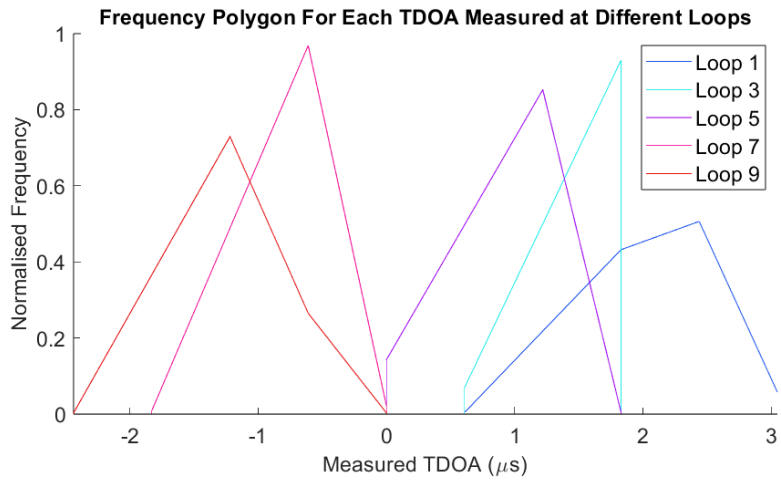


Figure 4.11: Normalised frequency polygons for the TDOA measurements at each loop made using thresholding. The signal was sampled and processed using the STM32 board.

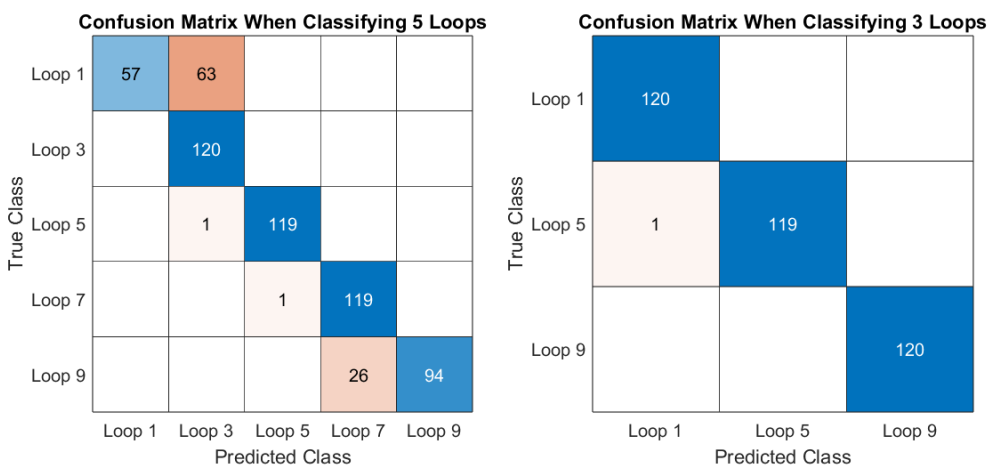


Figure 4.12: Confusion matrices which show how test data was classified by a decision tree. The TDOAs were measured using thresholding. The data was collected and processed using the STM32 board. The left confusion matrix used data from 5 loops, while the right matrix used data from 3 loops.

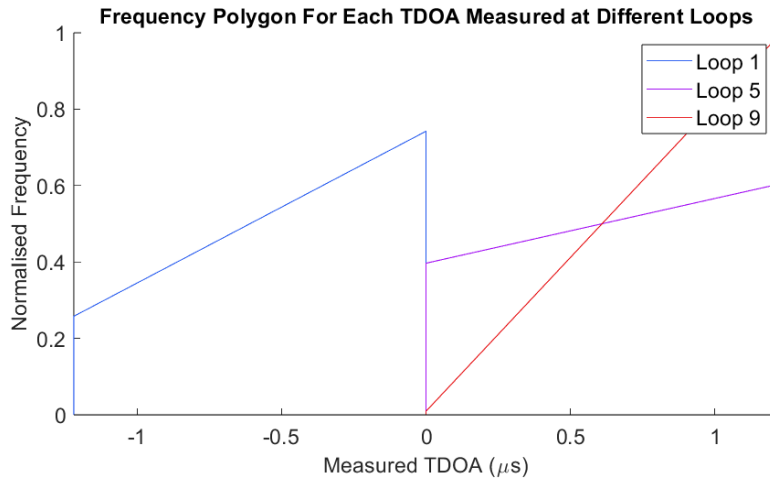


Figure 4.13: Normalised frequency polygon for the TDOA measurements at each loop made using cross-correlation. The signal was sampled and processed using the STM32 board.

sample difference between loop 1 and loop 9 of four, which is the value expected based on the sampling rate and true TDOA. However, the separation between loops is smaller than when thresholding was used to measure the TDOA. This is highlighted in the left confusion matrix of Figure 4.14, where an error rate of 33% occurs for a 3-class classification system. The right confusion matrix of Figure 4.14 shows that the error rate drops to 0 for a 2-class classification system.

The TDOAs measured using cross-correlation, more accurately represent the true TDOAs when compared with those measured using thresholding. This shows that cross-correlation is less affected by factors other than the distance travelled, resulting in a more robust and adaptable system, despite thresholding leading to better class separation. The thresholding system was conducted during the VICC's SOF and was completed before the VICC began transmitting the first bit of the message, while the cross-correlation system had to be conducted in parallel with the signal demodulation. Consequently, cross-correlation led to a substantial increase in the required processing time. This analysis therefore shows that if localisation is to be implemented in a practical application, a designer must carefully consider if thresholding or cross-correlation is optimal.



Figure 4.14: Confusion matrices which show how test data was classified by a decision tree. The TDOAs were measured using cross-correlation. The data was collected and processed using the STM32 board. The left confusion matrix used data from 3 loops, while the right matrix used data from 2 loops.

Conclusions

In this thesis, a VCD was implemented according to the ISO 15693 standard. The VCD transmitted an inventory request to the VICC, which responded with its UID. Seven methods of demodulation were tested, and the potential benefits of each were analysed. The VCD was then altered by replacing the single inductive loop with a travelling wave antenna that consisted of nine inductive loops. The TDOA between the outputs at either end of the antenna was used to estimate the VICCs position. The localisation and demodulation systems were initially implemented in MATLAB using data collected by a digital oscilloscope. Subsequently, all systems were implemented in C and loaded onto a STM32 NUCLEO F446RE development board.

The VICC transmits information via subcarrier load modulation. Consequently, two methods of demodulation could be applied: BPFs could isolate the subcarrier or sideband frequencies, or an analogue AM detector could produce a square wave caused by the load modulation. Although these methods could be combined, with a BPF applied to the signal output by an AM detector, this was found to provide no benefit to a receiver's performance.

Threshold, correlation and amplitude receivers were all tested to minimise the BER in signal demodulation. For the entirely digital detection systems the maximum read range was 8 cm obtained with a minimum error rate of 0.9% when using cross-correlation. However, the error rate for read ranges below 4 cm was minimised by implementing an amplitude receiver. When using the STM32 board, which undersampled the carrier wave by a factor of 13, a digital Butterworth filter was found to best isolate the lower sideband produced by the subcarrier. Due to a high level of interference, the upper sideband could not be isolated when using the STM32 board.

Introducing an analogue AM detector increased the read range of the NFC system from 8 cm to 11 cm, and resulted in a more reliable receiver for read ranges between 1 cm and 8 cm. Cross-correlation was found to result in a lower BER when compared with a threshold receiver. The largest read range was achieved when the cross-correlator did not use digital filtering, however, this also led to inconsistent performance at shorter read ranges. To smooth the signal into a more ideal square wave, a digital low pass filter was applied to the signal when using an AM detector.

The time difference between the outputs at either end of a travelling wave antenna allowed

a classification system to estimate which loop in the antenna the VICC was closest to. With a sampling rate of 10 MHz, the cross-correlation system resulted in a classification error rate of 3.06%. When higher sampling rates were used, the error rate did not decrease, but FDR increased, indicating that higher sampling rates result in a more robust classification system. Thresholding has a lower computational complexity than cross-correlation, however, when implemented to estimate the TDOA, the minimum error rate was 11% when classifying all nine loops, suggesting that fewer loops are required for reliable performance.

The thresholding and cross-correlation systems were tested using fewer loops of the travelling wave antenna, as this increased the change in TDOA between neighbouring loops. When only three of the nine loops were used, thresholding resulted in the lowest error rate and the highest FDR. This was validated when the localisation system was implemented on the STM32 board. The thresholding system assigned test data to the correct loop with an accuracy of 0.28 %, while the cross-correlation system had an accuracy of 33%, for three class systems. However, the TDOA measured using thresholding was more heavily influenced by factors other than the distance travelled, such as the transition gradients of the two square waves, indicating a less robust localisation system. The error rate for both systems decreased to zero when only two loops were used as classes.

The performance of the receivers was only tested when the ADC undersampled the carrier wave by a factor of 13. Testing the receivers for higher sampling rates could provide valuable insights on the optimal sampling rate for different applications. This project focused on digital receivers and digital filtering, therefore, adding bespoke analogue solutions would be an interesting addition to this work. A custom AM detector and more carefully designed analogue filters could be implemented to make a more effective hybrid system.

The localisation system used a power of only 0.25 watts, resulting in the vertical read range for consistent localisation to be 3 cm. Consequently, the localisation accuracy for different read ranges could not be analysed. For future work, increasing the power could extend the read range, enabling an analysis of how the separation distance between the VCD and VICC affects the measured TDOA.

NFC is a highly adaptable technology that can be applied to many facets of life. The bespoke system designed in this report can aid in the development of new applications, as it can be easily adapted for optimal performance in a wide variety of NFC systems.

A

Scattering Parameters of

Hardware

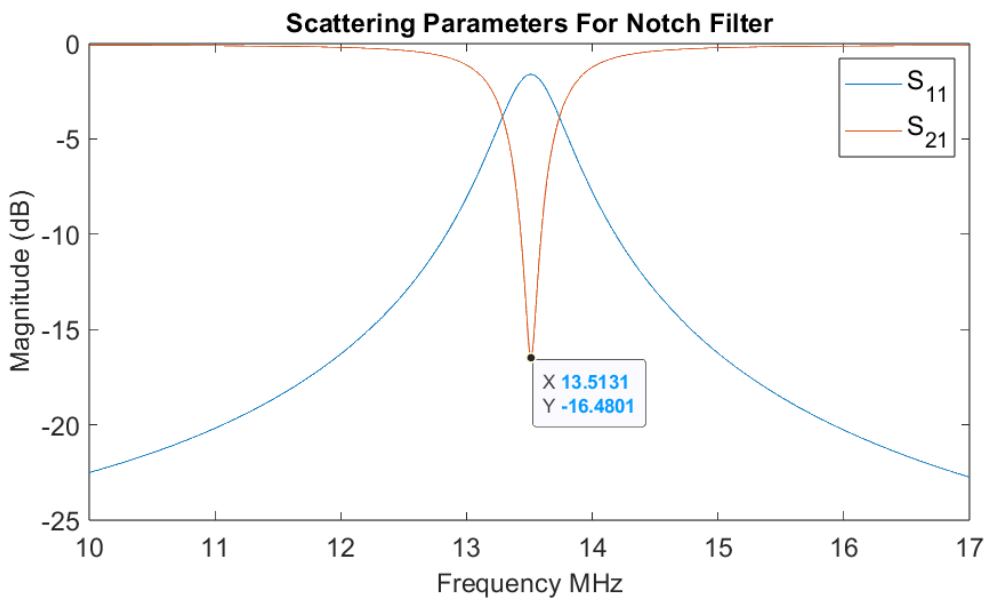


Figure A.1: Scattering parameters for notch filter

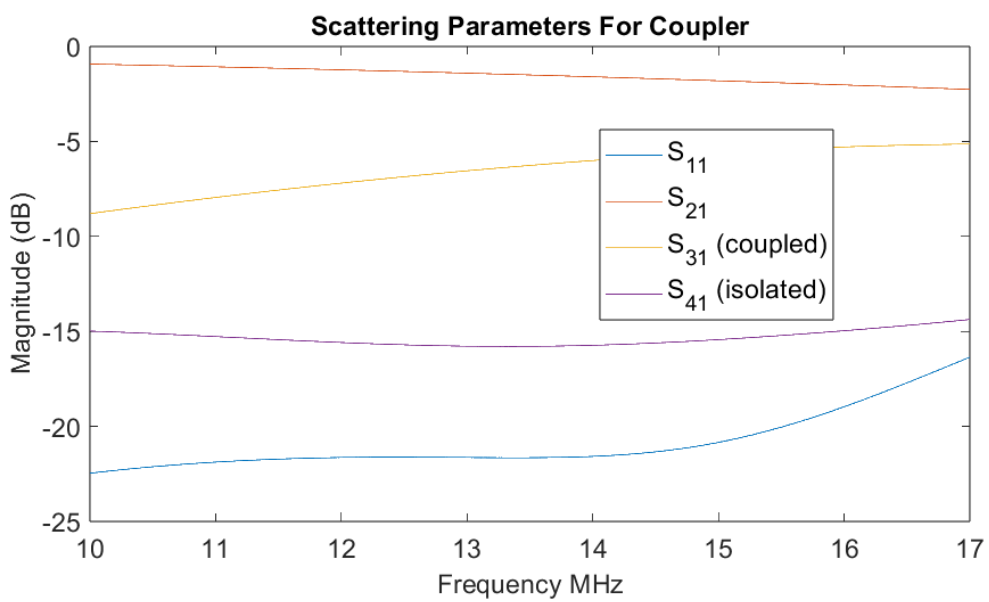


Figure A.2: Scattering parameters for coupler

A

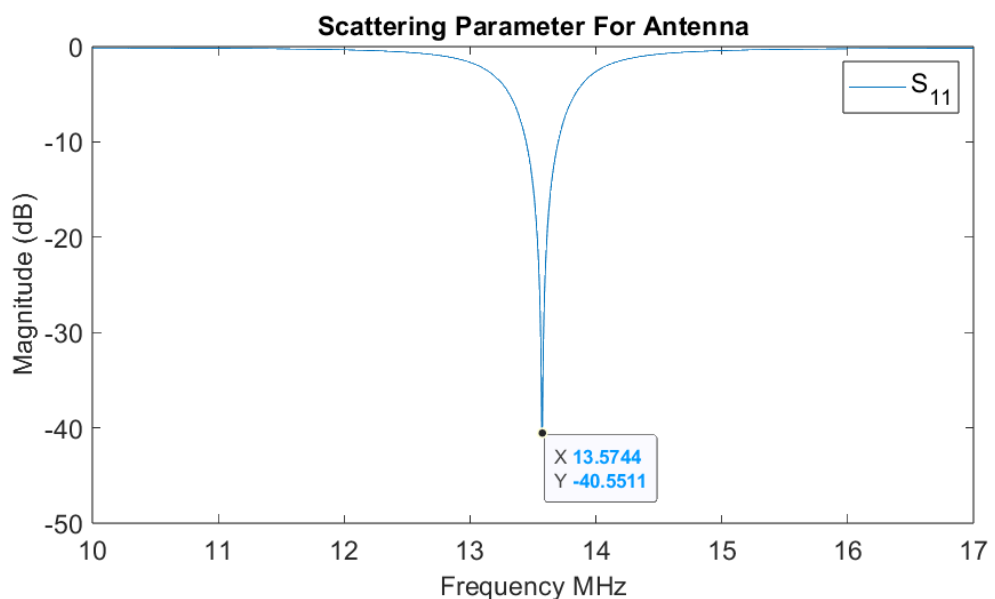


Figure A.3: Scattering Parameter for Antenna

Bibliography

- [1] A. Keyanfar, M. Roeintan, and K. Gheibi, “Monitoring weather condition based on near-field communication (nfc) system,” in *2022 14th International Conference on Mathematics, Actuarial Science, Computer Science and Statistics (MACS)*, 2022, pp. 1–8. DOI: 10.1109/MACS56771.2022.10022999.
- [2] J. Quignon, A. Tornambe, T. Deleruyelle, and P. Pannier, “Wireless charging using nfc technology,” in *2021 6th International Conference on Smart and Sustainable Technologies (SpliTech)*, 2021, pp. 1–4. DOI: 10.23919/SpliTech52315.2021.9566468.
- [3] E. M. Melchor-Martínez, R. Macias-Garbett, A. Malacara-Becerra, H. M. Iqbal, J. E. Sosa-Hernández, and R. Parra-Saldívar, “Environmental impact of emerging contaminants from battery waste: A mini review,” *Case Studies in Chemical and Environmental Engineering*, vol. 3, p. 100104, 2021, ISSN: 2666-0164. DOI: <https://doi.org/10.1016/j.cscee.2021.100104>. [Online]. Available: <https://www.sciencedirect.com/science/article/pii/S2666016421000268>.
- [4] C. Schuss, T. Leikanger, and J. Häkkinen, “Efficient external sensors for smartphones through near field communication (nfc),” in *2018 IEEE International Instrumentation and Measurement Technology Conference (I2MTC)*, 2018, pp. 1–6. DOI: 10.1109/I2MTC.2018.8409655.
- [5] X. Wang, Z. Zhou, Y. Li, and Z. Jin, “An efficient sports navigation method based on nfc technology,” in *2020 International Conference on Intelligent Transportation, Big Data Smart City (ICITBS)*, 2020, pp. 850–855. DOI: 10.1109/ICITBS49701.2020.00187.
- [6] E. A. Kadir, S. M. Shamsuddin, S. K. A. Rahim, and S. L. Rosa, “Application of nfc technology for premise halal certification,” in *2015 3rd International Conference on Information and Communication Technology (ICoICT)*, 2015, pp. 618–621. DOI: 10.1109/ICoICT.2015.7231497.
- [7] P. I. Tutubalin, “Method of increasing information security of petrochemical industry enterprises using nfc technology,” in *2021 International Conference on Industrial Engineering, Applications and Manufacturing (ICIEAM)*, 2021, pp. 576–580. DOI: 10.1109/ICIEAM51226.2021.9446396.

- [8] C. Saminger, S. Grünberger, and J. Langer, “An nfc ticketing system with a new approach of an inverse reader mode,” in *2013 5th International Workshop on Near Field Communication (NFC)*, 2013, pp. 1–5. DOI: [10.1109/NFC.2013.6482448](https://doi.org/10.1109/NFC.2013.6482448).
- [9] Y. Liu, C. Ouyang, Z. Wang, J. Xu, X. Mu, and A. L. Swindlehurst, *Near-field communications: A comprehensive survey*, 2024. arXiv: 2401.05900 [eess.SP]. [Online]. Available: <https://arxiv.org/abs/2401.05900>.
- [10] Y. Liu, Z. Wang, J. Xu, C. Ouyang, X. Mu, and R. Schober, “Near-field communications: A tutorial review,” *IEEE Open Journal of the Communications Society*, vol. 4, pp. 1999–2049, 2023. DOI: [10.1109/OJCOMS.2023.3305583](https://doi.org/10.1109/OJCOMS.2023.3305583).
- [11] K. T. Selvan and R. Janaswamy, “Fraunhofer and fresnel distances: Unified derivation for aperture antennas,” *IEEE Antennas and Propagation Magazine*, vol. 59, no. 4, pp. 12–15, 2017. DOI: [10.1109/MAP.2017.2706648](https://doi.org/10.1109/MAP.2017.2706648).
- [12] M. Cui, Z. Wu, Y. Lu, X. Wei, and L. Dai, “Near-field mimo communications for 6g: Fundamentals, challenges, potentials, and future directions,” *IEEE Communications Magazine*, vol. 61, no. 1, pp. 40–46, 2023. DOI: [10.1109/MCOM.004.2200136](https://doi.org/10.1109/MCOM.004.2200136).
- [13] R. R. A. Syms, O. Sydoruk, and M. C. K. Wiltshire, “Magneto-inductive hf rfid system,” *IEEE Journal of Radio Frequency Identification*, vol. 5, no. 2, pp. 148–153, 2021. DOI: [10.1109/JRFID.2020.3042719](https://doi.org/10.1109/JRFID.2020.3042719).
- [14] K. Finkenzeller and D. Müller, *RFID handbook : fundamentals and applications in contactless smart cards, radio frequency identification and near-field communication*, eng, 3rd ed. Chichester: Wiley, 2010, ISBN: 0470695064.
- [15] A. M. Elbir, K. V. Mishra, S. A. Vorobyov, and R. W. Heath, “Twenty-five years of advances in beamforming: From convex and nonconvex optimization to learning techniques,” *IEEE Signal Processing Magazine*, vol. 40, no. 4, pp. 118–131, 2023. DOI: [10.1109/MSP.2023.3262366](https://doi.org/10.1109/MSP.2023.3262366).
- [16] S. Kisseeff, I. F. Akyildiz, and W. Gerstacker, “Distributed beamforming for magnetic induction based body area sensor networks,” in *2016 IEEE Global Communications Conference (GLOBECOM)*, 2016, pp. 1–7. DOI: [10.1109/GLOCOM.2016.7841737](https://doi.org/10.1109/GLOCOM.2016.7841737).
- [17] S. Kisseeff, I. F. Akyildiz, and W. Gerstacker, “Beamforming for magnetic induction based wireless power transfer systems with multiple receivers,” in *2015 IEEE Global Communications Conference (GLOBECOM)*, 2015, pp. 1–7. DOI: [10.1109/GLOCOM.2015.7417006](https://doi.org/10.1109/GLOCOM.2015.7417006).

- [18] A. K. Abdulwahab and W. M. El-Medany, "Nfc payments security in light of covid-19 pandemic: Review of recent security threats and protection methods," in *2021 International Conference on Data Analytics for Business and Industry (ICDABI)*, 2021, pp. 615–620. DOI: [10.1109/ICDABI53623.2021.9655849](https://doi.org/10.1109/ICDABI53623.2021.9655849).
- [19] A. Zhao and F. Ai, "Dual-resonance nfc antenna system based on nfc chip antenna," *IEEE Antennas and Wireless Propagation Letters*, vol. 16, pp. 2856–2860, 2017. DOI: [10.1109/LAWP.2017.2749683](https://doi.org/10.1109/LAWP.2017.2749683).
- [20] L.-D. Forrester, R. Shaw, and S. Thorpe, "Assessing relay attacks in nfc enabled devices a three factor relay test environment (rate) approach," in *SoutheastCon 2018*, 2018, pp. 1–8. DOI: [10.1109/SECON.2018.8478914](https://doi.org/10.1109/SECON.2018.8478914).
- [21] R. Lyu, W. Cheng, W. Zhang, and F. Qin, "Oam-nfc: A short-range high capacity transmission scheme," in *ICC 2020 - 2020 IEEE International Conference on Communications (ICC)*, 2020, pp. 1–6. DOI: [10.1109/ICC40277.2020.9148881](https://doi.org/10.1109/ICC40277.2020.9148881).
- [22] D. Rinner, H. Witschnig, and E. Merlin, "Broadband nfc - a system analysis for the uplink," in *2008 6th International Symposium on Communication Systems, Networks and Digital Signal Processing*, 2008, pp. 292–296. DOI: [10.1109/CSNDSP.2008.4610713](https://doi.org/10.1109/CSNDSP.2008.4610713).
- [23] M. Gossar, M. Stark, M. Gebhart, W. Pribyl, and P. Söser, "Investigations to achieve very high data rates for proximity coupling devices at 13.56 mhz and nfc applications," in *2011 Third International Workshop on Near Field Communication*, 2011, pp. 71–76. DOI: [10.1109/NFC.2011.12](https://doi.org/10.1109/NFC.2011.12).
- [24] C. Degen, "Inductive coupling for wireless power transfer and near-field communication," *EURASIP Journal on Wireless Communications and Networking*, p. 121, 2021. DOI: <https://doi.org/10.1186/s13638-021-01994-4>.
- [25] C. Shannon, "Communication in the presence of noise," *Proceedings of the IRE*, vol. 37, no. 1, pp. 10–21, 1949. DOI: [10.1109/JRPROC.1949.232969](https://doi.org/10.1109/JRPROC.1949.232969).
- [26] Y. Zhao, "Standardization of mobile phone positioning for 3g systems," *IEEE Communications Magazine*, vol. 40, no. 7, pp. 108–116, 2002. DOI: [10.1109/MCOM.2002.1018015](https://doi.org/10.1109/MCOM.2002.1018015).
- [27] G. Sun, J. Chen, W. Guo, and K. R. Liu, "Signal processing techniques in network-aided positioning: A survey of state-of-the-art positioning designs," *IEEE Signal Processing Magazine*, vol. 22, no. 4, pp. 12–23, 2005. DOI: [10.1109/MSP.2005.1458273](https://doi.org/10.1109/MSP.2005.1458273).

- [28] L. M. Ni, D. Zhang, and M. R. Souryal, “Rfid-based localization and tracking technologies,” *IEEE Wireless Communications*, vol. 18, no. 2, pp. 45–51, 2011. doi: [10.1109/MWC.2011.5751295](https://doi.org/10.1109/MWC.2011.5751295).
- [29] K. Yamano, K. Tanaka, M. Hirayama, E. Kondo, Y. Kimuro, and M. Matsumoto, “Self-localization of mobile robots with rfid system by using support vector machine,” in *2004 IEEE/RSJ International Conference on Intelligent Robots and Systems (IROS) (IEEE Cat. No.04CH37566)*, vol. 4, 2004, 3756–3761 vol.4. doi: [10.1109/IROS.2004.1389999](https://doi.org/10.1109/IROS.2004.1389999).
- [30] Y. Senta, Y. Kimuro, S. Takarabe, and T. Hasegawa, “Machine learning approach to self-localization of mobile robots using rfid tag,” in *2007 IEEE/ASME international conference on advanced intelligent mechatronics*, 2007, pp. 1–6. doi: [10.1109/AIM.2007.4412485](https://doi.org/10.1109/AIM.2007.4412485).
- [31] L. Xu, J. Liu, X. Wang, H. Gong, Y. Wang, and L. Chen, “Hf rfid-based book localization via mobile scanning,” in *2020 17th Annual IEEE International Conference on Sensing, Communication, and Networking (SECON)*, 2020, pp. 1–9. doi: [10.1109/SECON48991.2020.9158442](https://doi.org/10.1109/SECON48991.2020.9158442).
- [32] Y. Mehlman, P. Kumar, M. Ozatay, S. Wagner, J. C. Sturm, and N. Verma, “Large-area electronics hf rfid reader array for object-detecting smart surfaces,” *IEEE Solid-State Circuits Letters*, vol. 1, no. 8, pp. 182–185, 2018. doi: [10.1109/LSSC.2019.2902063](https://doi.org/10.1109/LSSC.2019.2902063).
- [33] A. S. Khan and S. K. Mukerji, “Electromagnetic waves,” eng, in *Electromagnetic Fields*, 1st ed., vol. 1, United Kingdom: CRC Press, 2021, pp. 559–590, ISBN: 036749499X.
- [34] R. R. A. Syms, A. Voronov, and O. Sydoruk, “Hf rfid tag location using magneto-inductive waves,” *IEEE Journal of Radio Frequency Identification*, vol. 6, pp. 347–354, 2022. doi: [10.1109/JRFID.2022.3182894](https://doi.org/10.1109/JRFID.2022.3182894).
- [35] A. Voronov, O. Sydoruk, and R. R. A. Syms, “Waveguide antenna topologies for distributed high-frequency near-field communication and localization,” *IEEE Transactions on Antennas and Propagation*, vol. 71, no. 6, pp. 5026–5035, 2023. doi: [10.1109/TAP.2023.3263928](https://doi.org/10.1109/TAP.2023.3263928).
- [36] “Cards and security devices for personal identification. contactless vicinity objects. anti-collision and transmission protocol,” British Standards Institution, Standard BS ISO/IEC 15693-3, 2019.
- [37] “Cards and security devices for personal identification. contactless vicinity objects. air interface and initialization,” British Standards Institution, Standard BS ISO/IEC 15693-2, 2019.

- [38] “Cards and security devices for personal identification — contactless proximity objects,” British Standards Institution, Standard BS ISO/IEC 14443, 2019.
- [39] S. Theodoridis, “Chapter 7 - classification: A tour of the classics,” in *Machine Learning (Second Edition)*, S. Theodoridis, Ed., Second Edition, Academic Press, 2020, pp. 301–350, ISBN: 978-0-12-818803-3. DOI: <https://doi.org/10.1016/B978-0-12-818803-3.00016-7>. [Online]. Available: <https://www.sciencedirect.com/science/article/pii/B9780128188033000167>.